Istanbul Medipol University
School of Engineering and Natural Sciences
Graduation Project Report 1
2024 - 2025

PROJECT TITLE
Odor Discrimination via Neural Frequency and Vibration Analysis
PROJECT ADVISOR
Prof. Dr. Mehmet Kemal ÖZDEMİR
TEAM MEMBERS
Ali Zareh Matin Hassanloo İbrahim Davutoğlu

Istanbul Medipol University
School of Engineering and Natural Sciences
Graduation Project 2 Report

Project Code

Project Title:

Odor Discrimination via Neural Frequency and Vibration Analysis

Project Advisor:

Prof. Dr. Mehmet Kemal ÖZDEMİR

Project Team Members:

Matin Hassanloo (Representative) - Ali Zareh - İbrahim Davutoğlu

Sponsor Company (If any):

TÜBİTAK 2209A - Medipol REMER Lab (Q Laboratory) - KU Leuven Nerf Lab

BUDGET (TL)	PROPOSED	CONSENTED
IMU FUNDING	7000	7000
SPONSOR COMPANY FUNDING	9000	9000
TOTAL	16000	16000

PROJECT PLAN	PROPOSED	CONSENTED
PROJECT PLAN Duration in Weeks	28 Weeks	28 Weeks
STARTING DATE	11.10.2024	11.10.2024

Istanbul Medipol University
School of Engineering and Natural Sciences
Graduation Project 2 Report

Project Code	

PROJECT ADVISOR	**DEPARTMENT CHAIR**
Name: Mehmet Kemal Özdemir	**Name:** Mehmet Kemal Özdemir
Contact Information: Tel: E-mail: mkozdemir@medipol.edu.tr	**Contact Information:** Tel: E-mail:
Signature:	**Signature:**

TEAM MEMBER	**TEAM MEMBER**
Name: Matin Hassanloo	**Name:** İbrahim Davutoğlu
Contact Information: Tel: E-mail: matin.hassanloo@std.medipol.edu.tr	**Contact Information:** Tel: E-mail: ibrahim.abou@std.medipol.edu.tr
Signature:	**Signature:**

TEAM MEMBER	**SPONSOR COMPANY**
Name: Ali Zareh	**Name:** TÜBİTAK
Contact Information: Tel: E-mail: ali.zareh@std.medipol.edu.tr	**Contact Information:** Tel: - E-mail: -
Signature:	**Signature:**

Istanbul Medipol University
School of Engineering and Natural Sciences
Graduation Project 2 Report

Project Title: Odor Discrimination via Neural Frequency and Vibration Analysis

Project Advisor: Prof. Dr. Mehmet Kemal ÖZDEMİR

Team Members: İbrahim Davutoğlu - Matin Hassanloo - Ali Zareh

Project Group Title: Odor Discrimination

PROJECT ABSTRACT

Odor detection is critical for food safety, environmental monitoring, and medical diagnostics. Current artificial sensors struggle with real-time odor identification, and chemical sensors fail to resolve complex odorant mixtures, leaving physiological recordings from living bodies as the primary analysis tool. Existing electronic-nose technologies, which mostly rely on fixed chemical sensors, perform adequately under controlled conditions but lack the real-time adaptability and specificity required to discriminate complex odors.

In this project, we utilized multi‑channel electrophysiological recordings from the mouse olfactory bulb (OB) and piriform cortex (PCx) to validate the molecular‑vibration hypothesis and to develop AI models capable of decoding odor identity directly from neural signals. Across 3,745 inhalation‑locked trials in seven mice, six chemically diverse odorants and blank (mineral‑oil) controls were delivered while local field potentials (LFPs) were sampled at 30 kHz. Signals were down‑sampled to 1000 Hz and reduced via PCA into "master‑channel" waveforms. We extracted canonical band‑power features (δ through high‑γ) using Welch's periodogram and continuous Morlet wavelet transforms, and we compiled FTIR and Raman vibrational fingerprints for each odorant.

Building on these datasets, we designed and tuned deep‑learning architectures. Two complementary one‑dimensional CNNs—ResCNN and AttentionCNN—were trained to detect odor presence versus blank trials, achieving an ensemble accuracy of 83 %, sensitivity of 76%, specificity of 92%, and AUC = 0.89 on 2,349 OB trials. We then developed

Istanbul Medipol University
School of Engineering and Natural Sciences
Graduation Project 2 Report

DualRegionNet, a dual‑branch CNN with spatial‑attention modules that fuses OB and PCx embeddings for multiclass odor discrimination. Under five‑fold cross‑validation, the final ensemble yielded 90.5% accuracy on a four‑class set and 80.5% on the full seven‑class panel. Targeted ablations confirmed that theta‑band inputs, dual‑region fusion, and attention mechanisms each contribute ≥ 3–7 percentage‑point gains.

We implemented bidirectional Random Forest regressors: forward models (FTIR → neural band‑power) achieved $R^2 > 0.72$, while reverse models (neural → FTIR) yielded $R^2 > 0.70$, demonstrating robust mapping between molecular vibrational spectra and brain oscillations. Feature‑importance analyses revealed that delta and beta bands best predict carbonyl, whereas theta and alpha bands encode C–H vibrations.

Our results validate a comprehensive, spectro‑neural framework for odor decoding by demonstrating that multi-region LFP features can substitute for labor-intensive spike sorting in real-time odor classification. Our attention-based DualRegionNet and odor presence models achieve high accuracy > 80% across complex odor panels and meet our success criteria. The findings serve as a normative framework for analyzing multi-region recordings, with applications in neural decoding, brain-machine interfaces, and show the capability of deep learning (DL) approaches in detecting the presence of odors from neural activity.

Keywords: Odor Discrimination, Neural Data, Molecular Vibration, Frequency Transmission

1. OBJECTIVE OF THE PROJECT:

The ultimate aim and goal of this project is to establish a comprehensive framework for encoding, transmitting, and regenerating olfactory information in a manner similar to digital audio and visual signals. By the conclusion of our work, we demonstrated that it's completely possible to capture live neural activity evoked by odorants, extract spectral and temporal features, and reconstruct synthetic scent signatures through artificial intelligence based models. This lays the foundation for new generation olfactory interfaces such as electronic noses for environmental or food safety monitoring to immersive virtual reality systems capable of delivering realistic scent

experiences. To meet this ambition, we pursued three interrelated sub-objectives, each of which we met throught targeted experiments and analyses:

We developed and validated end-to-end deep-learning models (ResCNN, AttentionCNN, and DualRegionNet) that decoded odor identity and presence directly from multi-channel singals recorded in the mouse OB and PCx. By applying Welch's overlapped-segment method, wavelet transforms, and generative augmentation (GAN), we achieved up to 90% precision on four-class odor discrimination, 83% accuracy for binary odor detection, and 70% accuracy on seven-class tasks. These results confirmed that our system recognizes odors in real time and on single trials with performance that surpasses conventional spike-sorting or offline approaches.

We examined how specific chemicals within odorants—characterized by Fourier-transform infrared (FTIR) spectroscopy—are encoded in neural oscillatory patterns. Through bidirectional random forest regression analyses, we demonstrated that functional-group absorbances (e.g., C=O, C–H, C–O stretches) predicted band-power fluctuations in delta through high gamma ranges, and conversely, that neural frequency profiles could reconstruct FTIR spectra. This confirmed, for the first time with real electrophysiological data, that molecular-vibration theory underlies olfactory encoding in living circuits.

In partnership with KU Leuven's NERF Lab, we established Medipol Remer Lab as Turkey's first facility capable of high-fidelity, electrophysiological odor-evoked recordings. Collectively, these accomplishments demonstrate that neural signals can be algorithmically mapped to chemical structure and back, allowing the digital transmission and synthetic reconstruction of odors. In the years following project completion, our platform will support practical tools such as electronic noses for environmental and medical diagnostics, and scent-enabled virtual-reality or telepresence systems that restore or augment human olfactory experience.

2. LITERATURE REVIEW:

The ability to understand and discriminate a vast and chemically diverse array of odorants underlies many essential behaviors—ranging from food safety, environmental monitoring, predator avoidance to social communication and medical diagnostics. Yet, the olfactory system's combinatorial coding of vast chemical spaces presents profound challenges for both experimental characterization and computational modeling. In this literature review, we first introduce the principal theoretical concepts and approaches that have shaped today's understanding of odor discrimination and and subsequently examine key contributions across different thematic domains, that have been our main area of study throughout the project.

Two well-known models have guided research on how odorant molecules interact with the olfactory system. The "lock-and-key" framework *(also known as the shape theory)* proposes that the shape of a molecule fits into receptor binding much like a key fits into a lock. On the other hand, the molecular vibration hypothesis indicates that the vibrational energy levels of odorant molecules drive receptor activation and ultimately shape odor perception. While each theory is supported by experimental and computational studies, neither fully captures the complexity of mixture effects or context-dependent perception. This review therefore adopts an integrative perspective, drawing on evidence from both chemical and biological domains.

Recent technological and methodological advances have expanded our ability to probe odor coding at multiple scales. On the neural side, multi-channel electrophysiological recordings combined with deep neural networks can decode odor representations directly from brain activity. Time–frequency analyses, including wavelet transforms and Welch's method, further reveal how oscillatory signals in theta, beta, and gamma frequency bands contribute to discrimination. Meanwhile, high-resolution spectroscopic techniques (FTIR and Raman) provide detailed vibrational fingerprints of odorant molecules, enabling correlations between chemical structure and receptor responses. Studies of odor mixtures then explore whether combining base compounds yields additive, suppressive, or emergent percepts.

In the following, we organize our literature review into **four** different domains, starting from the fundamental concepts to specialized methodologies. **Section 1** introduces the theoretical founrdation of olfactory coding, contrasting the shape and molecular vibration theories and examining comparative analysis of both methods. Additionally, we will discuss how the vibrations are a function of the chemical bonds. **Section 2** evaluates the EEG recordings and their limitations for high-frequency signals, the spatial and temporal advantages of LFP and single unit recordings. **Section 3** covers studies based on spike sorting and basic feature extraction *(firing rates, band powers)*, classical classifiers *(LDA, SVMs, threshold methods)*, as well as electronic nose *(e-nose)* architectures and their performance. **Section 4** reviews time-frequency based feature-extraction methods, including the wavelet transformers and Welch's periodogram applied to θ, β, and γ oscillations and compares their classification performance. This logical progression, from broad theory to targeted techniques and complex phenomena, will both contextualize our approach and highlight the critical gaps our project seeks to address.

2.1. *Section 1: Understanding the molecular shape and vibration theories in depth*

Woo and Roux present a strict computational framework in order to calculate the absolute binding energies of flexible ligands that are interacting with protein receptors by combining molecular dynamics and potential of mean force (PMF) techniques (Baumann, 2023). They decompose the binding process into sequential stages: (1) conformational restraining of the ligand to its bound-state geometry, (2) orientational and positional biasing into the receptor pocket, and (3) full release of those restraints within the binding site. Each step's free-energy change is computed explicitly, including the costs of losing conformational, translational, and rotational entropy, as well as the favorable interactions gained upon complex formation. This approach deepens our understanding of how molecular shape and flexibility affect receptor binding in olfaction. Just exactly as odorants must adopt specific three dimensional poses to fit into olfactory-receptor pockets and displace water molecules (Woo & Roux, 2005).

Chang and colleagues demonstrate that highly selective "lock-and-key" assembly can arise purely from particle geometry and environmental conditions, without requiring any specific chemical interactions. They modeled spherical key particles fitting into the lock cavities. Both the keys and locks were placed in a liquid filled with non-adsorbing polymer chains. The so called setup allows them to understand and study how the lock and key interactions are influenced by the polymer environment that surrounds them. Since the polymers are not able to enter the narrow gap between lock and key, an osmotic imbalance drives the two colloids together. They have varied the polymer concentration and the chain length to quantify the free energy that is required to separate the lock and key pair, as well as the equilibrium fraction of bound pairs. The results reveal that increasing polymer concentration, and using solvents that improve polymer swelling all strengthen the binding between the lock-and-key and increase the proportion of bound colloids. Such findings underscore that, in addition to chemical contacts, the steric fit and local environment critically modulate molecular recognition in smell (Chang et al., 2015).

The authors designed one tweezer with a rigid spacers that hold its two arms in a fixed parallel position, so guests fit perfectly without forcing the host to change shape *("lock-and-key model")*. The second tweezers uses a more flexible spacer, so it must bend its arms around the guest, following an induced-fit model that costs energy. To

compare their performance, the researchers gradually added different planar molecules to a solution of each host and measured how the host's proton signals shifted, then fitted the data to identify binding strength. They could discover that the rigid tweezers bind up to ten times more strongly, since they do not pay the energetic penalty of reshaping, while the flexible host shows weaker binding. This study gives us a clean and synthetic example of the same basic principle that governs the interactions between the odorants and receptors in the nose. In olfaction, an odorant molecule should fit into the pocket of a receptor with the right and correct shape to trigger a signal. In other words, although gold tweezers aren't biological smell receptors, they clearly show that molecular shapes are the key criteria of synthetic and natural host–guest chemistry, including how we perceive smells. (Ibáñez & Peris, 2023).

Across the studies, we can clearly see lock-and-key recognition studied at different scales and levels of detail: Woo and Roux provide an atomistic free-energy breakdown by showing how a ligand's precise conformation, orientation, and entropy costs affect binding in a real protein pocket; on the other hand, Chang et al. use coarse-grained colloidal lock and key particles plus nonadsorbing polymers to demonstrate that pure shape complementarity and crowding can drive highly selective assembly without any specific chemical bonds; and Ibáñez and Peris use small tweezers to contrast a rigid lock-and-key host with a flexible induced-fit host, showing how host rigidity versus conformational change modulates binding strength. Overall, these studies, from full atomistic details, through entropic colloidal analogues, to minimal synthetic systems, deepen our knowledge of how molecular shape and environment dictate binding; having established this, we now turn to the molecular vibration hypothesis of olfaction, which proposes that the interactions between receptor and odorants also depend on vibrational energy matching.

Having established how three-dimensional shapes guide odorant binding, researchers have turned to studying how vibrational signatures complement these structural cues. Yan et al. introduce a specific spectroscopy as a uniquely label-free method for directly measuring the detailed vibrational signatures of biomacromolecules at interfaces. By overlapping infrared and visible laser pulses at a buried interface, they isolate only the second-order nonlinear signal generated where inversion symmetry is broken and, through careful polarization schemes, selectively extract the chiral tensor

elements that report on vibrational modes such as amide I and N–H. Their work shows that these chiral SFG signals can distinguish α-helices from β-sheets and monitor folding or self-assembly kinetics in real time, all without interference from bulk water (Yan et al., 2015). For olfaction, this technique demonstrates how the vibrational modes of odorant molecules—and their chiral arrangements when bound at receptor interfaces—can be directly probed under physiologically relevant conditions, showing the critical role of interfacial vibrational chirality in molecular recognition (Yan et al., 2014)

While shape theory explains how odorants fit into receptor pockets, electrophysiological recordings of OB reveal that odorant‑evoked glomerular activity is not randomly distributed but organized into spatial chemotopic maps. Neighboring glomeruli respond to molecules sharing both three‑dimensional features and vibrational characteristics. In order to understand what are glomeruli briefly, they are brain structures in the OB that process odor signals from the nose, to organize odors by their molecular features. In particular, Soelter et al. demonstrated through machine‑learning analysis of calcium‑imaging data that including computed vibrational descriptors alongside traditional shape metrics markedly enhances the prediction of which glomeruli will activate. Moreover, they found that glomeruli tuned to long‑chain aliphatics form distinct spatial clusters, indicating that variations in carbon‑chain length and specific functional groups interact with vibrational signatures to define receptor specificity at the early stages of olfactory processing (Soelter et al, 2020)

In accordance with the longstanding debate over whether odor discrimination is driven primarily by molecular shape or by vibrational spectra, Pandey et al. have demonstrated that a molecule's structure and its vibration are actually two sides of the same coin in determining odor perception. Using Chemical Graph Theory, they treat each odorant as a weighted graph—atoms as nodes and bonds as edges—to derive a Dynamical Matrix whose eigenvalues yield the molecule's vibrational pseudo‑spectrum *(the EigenVAlue, or EVA, descriptor)*. They then introduce a Peak‑Decomposed EVA *(PD‑EVA)* that distills this complex spectrum into a handful of physically meaningful vibrational peaks. By applying spectral clustering to PD‑EVA across twenty odorants spanning six perceptual classes, they recreate human odor categories—and even reveal natural subclasses—solely from vibrational data. This approach confirms that vibrational signatures inherently encode three‑dimensional shape information *(via the graph‑based*

Laplacian) while also capturing mode‑specific energetic features, unifying shape‑based "lock‑and‑key" docking models with vibration‑based sensing hypotheses. Unlike purely geometric models, which can struggle with molecules of similar shape, and unlike bulk vibration classifiers that ignore structural connectivity, Pandey et al.'s graph‑informed vibrational descriptors offer a predictive framework for how both shape and molecular vibrations together affect odor discrimination (Pandey et al., 2021).

Even if two odorants share the same three‑dimensional framework, their mirror image forms can smell strikingly different, indicating the limits of shape-only based theories. Saini and Ramanathan, examined specific cases such as carvone *(spearmint versus caraway)* and limonene *(citrus versus herbal)* to demonstrate that despite having identical geometries and shapes, these enantiomeric pairs elicit different olfactory perceptions. By integrating vibrational spectra with structural descriptors in a classification method, they could show that key differences in vibrational mode intensities, specifically in C-H bending and streching regions are important to correctly discriminate each enantiomer's smell. This analysis reveals that olfactory receptors *(ORNs)* not only recognize steric complementarity but also respond to subtle shifts in molecular vibrations. This gives a clear and full understanding of odor detection being accounted to both shape and vibrational signatures (Saini & Ramanathan, 2022).

Ameta and Durgesh have worked on the prediction of odors using vibrational spectra. We know that machine learning and deep learning algorithms are useful to help us learn more about the properties of odor molecules. Since it is possible to have more accurate predictions for different smell by converting vibration data to the computer analyzable features, the models that have both of vibration information and the molecule's shape could outperform older and traditional methods. That being said, it is a proof that both of these mentioned factors are pretty important in studying smells. As as example, scientists in this research used some complicated clustering and image based deep learning method on the vibration data. Their classification results were also improved by using simplification techniques, such as PCA and t-SNE. (Ameta et al.)

Another important aspect of odor discrimination studies, is dealing with how functional groups and chain length could affect smell. Scientists in this study measured the shapes of molecules according to their functionality and carbon chains, to see how these components are related to a smell. Each of these chemical groups and the chain lengths are recognizable by our olfactory cells in the noses. Some cells are specially sensitive to long carbon chains. This evidence about the Shape Theory indicates that the shape of molecule is related to the odor it releases. The other theory is that the vibration of the molecules could help to activate these specific types of cells. Other studies found that cells sensitive to n-fatty acids and n-aliphatic alcohols are sensitive to specific chain lengths. This would indicate that the vibration, along with the structure of each molecule, is responsible for identifying and processing smells. (Pandey et al.; Soelter et al.).

The same scientists that worked on predicting odors through vibrations, have also studied and explored the methods and techniques for handling vibration data. In this paper they are analyzing how vibration data is used to transform the vibrational spectra to machine learning features. Firstly, they have cleaned up the spectra by using Gaussian smoothing and then they reduced the number of features using PCA. As mentioned in the paper, they face class imbalance during their work, so they are using a cost sensitive multilayer perceptron model. Additionally, as some alternative approaches, random over and undersampling are being use which could help the outcome from binary classification to be improved. Successfully, the methods of combining vibration information with other molecular properties resulted in models that were excellent for odor classification. (Ameta et al., "Odor Classification").

Having all these studies together, it is quite clear that molecular recognition in olfaction emerges from an intricate interplay of three-diemsional shape and vibrational dynamics. Yan et al. establish that chiral vibrational SFG spectroscopy can directly resolve interfacial conformations and stereochemistry, while Soelter et al. show that by combining vibrational descriptors with shape metrics improves prediction of spatially organized glomerular responses in the OB. Pandey et al., on the other hand, unify these perspectives by demonstrating that graph-informed vibrational spectra inherently encode both shape topology and mode-specific energetics and it offers predictive framework for how both shape and molecular vibrations together affect odor discrimination. Saini and Ramanathan further reveal that enantiomeric odorants, can be discriminated only by

integrating subtle vibrational differences with structural descriptors. Finally, Ameta et al. scale these insights to thousands of molecules, showing that deep‑learning models trained on image‑encoded vibrational spectra fused with molecular fingerprints substantially outperform structure‑only classifiers. Collectively, these findings indicate that neither shape nor vibration alone suffices.

As we have reviewed how both precise three-dimensional fits and intrinsic vibrational fingerprints jointly govern odorant recognition—from atomistic free-energy landscapes and coarse-grained lock-and-key analogues, through chiral interfacial spectroscopy and spatially organized glomerular maps, to graph-informed clustering and large-scale deep learning—we now possess a unified framework for understanding the molecular determinants of smell. With this foundation in place, Section 2 will turn to the neural signatures of olfaction, examining how electroencephalography *(EEG)* and related techniques capture the brain's real-time responses to these shape- and vibration-encoded olfactory cues.

2.2. *Section 2: Fundamental of EEG, limitations and Head-to-head comparisons*

Huart et al. applied non‑invasive EEG combined with time–frequency analysis to capture human olfactory cortical dynamics with high sensitivity. Using an automated olfactometer to deliver brief odor pulses, they recorded scalp EEG over frontal and central sites in awake volunteers and first attempted conventional event‑related potential averaging, which yielded little discernible signal due to temporal jitter and low signal‑to‑noise. They then computed single‑trial Morlet wavelet transforms to extract both phase‑locked and non–phase‑locked activity, revealing a robust theta‑band power increase *(3–7 Hz)* peaking 300–800 ms after odor onset and a concurrent alpha‑band desynchronization *(8–12 Hz)* extending to 1500 ms. The magnitudes of these spectral perturbations correlated significantly with individual psychophysical olfactory scores *(threshold, discrimination, identification)*, and a simple classifier using these features distinguished odor versus blank trials above chance. By showing that EEG oscillations in specific frequency bands reliably track odor perception and behavioral performance, this work provides a powerful, non‑invasive paradigm for studying human olfaction and for potentially diagnosing olfactory dysfunction (Huart et al., 2012).

Masaoka et al. use both EEG and fMRI to map the spatiotemporal cascade of olfactory processing in awake humans. By triggering EEG source analyses on inspiration onset and, in separate sessions, delivering brief odor pulses during fMRI, they show that EEG dipole modeling first localizes transient activity to primary olfactory structures—parahippocampal gyrus and amygdala—around 50 ms post‑inhalation, then to secondary association regions in the orbitofrontal cortex between 150 and 300 ms. Complementary fMRI activations converge on those same OFC loci, validating the EEG/DT estimates and confirming that inspiration‑locked EEG can non‑invasively resolve the rapid, hierarchical engagement of olfactory networks. This combined EEG–fMRI approach thus establishes both the temporal precision and spatial credibility of EEG measures for human odor detection, underpinning their use as reliable biomarkers of olfactory function (Masaoka et al., 2014).

Schriever et al. employed a low-cost, portable olfactometer combined with continuous Morlet wavelet time–frequency analysis to quantify odor-induced EEG-power changes in humans. Across three experimental phases, they first optimized stimulus parameters—finding that 1 s cued odor pulses with 18–20 s intertrial intervals maximized low-frequency *(2–6 Hz)* power responses—and then demonstrated that these EEG-power modulations at Cz reliably distinguished healthy controls from hyposmic and anosmic patients *(sensitivity 75%; specificity up to 89%)*, with effect sizes correlating with psychophysical TDI scores. Moreover, they confirmed good test–retest reliability over intervals up to two months. By showing that clinically feasible, non-invasive EEG time–frequency metrics can objectively assess central olfactory function and diagnose dysfunction, this work bridges sophisticated research protocols and routine clinical testing (Schriever et al., 2017)

Kum et al. employ an olfactory oddball paradigm in anesthetized mice to invasively record local LFPs simultaneously from 4 different regions including the olfactory epithelium *(OE)*, OB, prefrontal cortex *(PFC)*, and hippocampus *(HC)*. They demonstrate that both low-frequency *(delta and theta)* and high-frequency *(beta and gamma)* oscillations are robustly evoked by infrequent “deviant” odor presentations and that these responses persist in peripheral and central sites—with the hippocampus showing only transient onset responses. Mice rendered anosmic via $ZnSO_4$ treatment exhibit a profound loss of odor-evoked oscillatory power across all bands and regions,

confirming that these LFP signatures are specifically tied to functional olfactory input. As one of the limitations, LFPs recorded directly from the epithelium, bulb, and cortex have far higher spatial resolution and signal-to-noise ratio than scalp EEG; thus, the spectrally rich odor-evoked oscillations observed here may be attenuated or smeared when measured noninvasively through the human skull. This study provides compelling evidence that EEG related oscillations in frequency bands could be served as objective biomarkers for assessing olfactory function and dysfunction in humans (Kum et al., 2019)

Across these EEG investigations, a clear picture emerges of how time–frequency analysis can harness EEG's millisecond precision and, when combined with source modeling or complementary imaging, provide meaningful spatial insights into human olfaction. Huart et al. demonstrate that Morlet wavelet transforms reliably recover theta- and alpha-band odor-evoked oscillations even when traditional ERPs fail. Masaoka et al. then augment this temporal fidelity with spatial specificity by integrating EEG source localization and fMRI, mapping the rapid (50–300 ms) progression of activity from primary olfactory regions to orbitofrontal cortex. Schriever et al. show that a minimal, portable EEG montage can capture low-frequency power changes (2–6 Hz) that distinguish normosmic from impaired individuals with high reliability. Finally, Kum et al. show that invasive LFP recordings capture both low and high-frequency odor-evoked oscillations across peripheral and central olfactory sites. These studies show EEG's balance of temporal resolution and scalable coverage for odor discrimination. We now turn to a critical topic: EEG's inherent and natural challenges in detecting high-frequency rhythms and signals from the OB.

Iravani et al. and Ninenko et al. both have done non-invasive EEG probing in human olfactory processing, yet each highlights critical methodological hurdles related to scalp recordings. Iravani and colleagues developed the "electrobulbogram" (EBG) by positioning micro-amplified electrodes at the nasal bridge to isolate a gamma-band (~55–65 Hz) synchronization 100 to 150 milli-seconds after sniff onset and demonstrate its test–retest reliability, resistance to habituation, and absence in a congenitally anosmic individual (Iravani et al., 2020). Ninenko and co-workers, employed an instructed-delay paradigm with synchronized 19-channel EEG and nasal airflow monitoring to extract a 10–12 Hz inhalation-locked component that reliably differentiates odor versus odorless trials and precedes motor responses, alongside an ERP P200 marker of odor

identification. Both teams, however, mention significant EEG‑specific constraints: the EBG's proximity to facial muscles and eyes results in severe artifact contamination (over 50 % trial rejection), and its focus on high‑frequency oscillations may miss relevant low‑frequency dynamics; similarly, Ninenko et al. report that inconsistent alpha/theta findings across studies, manual versus automated odor delivery timing imprecision, inhalation‑trigger algorithm failures, and reliance on a single midline component in only a subset of participants all limit the generalizability and signal fidelity of their cortical markers. (Iravani et al., 2020; Ninenkoet al., 2022).

Now that we have highlighted EEG's challenges and limitations in capturing high frequency signals with conventional methods, we now turn to the comparison of non-invasive and invasive recordings. Yokoyama et al. present a novel deep-learning method for non-invasive electrophysiological source imaging *(ESI)* that is capable of localizing both cortical and subcortical generators of EEG signals. By training a four-layer convolutional neural network (CNN) on hundreds of realistic EEG forward simulations, they showed that 4LCNN achieves mean localization errors below 10 mm across signal‑to‑noise ratios typical of human EEG recordings. Head-to-head comparisons reveal that 4LCNN not only outperforms methods like eLORETA and LCMV in simulation but also localizes independent MEG‑derived to within 7-10 mm of their most correlated intracranial electrodes—distances comparable to the electrode spacing of SEEG grids. These results how that, by dramatically narrowing the gap between scalp EEG and invasive recordings, advanced deep-learning methods could soon enable reliable, non-invasive mapping of odor‑related structures *(e.g., the OB or PCx)* during olfactory tasks, thus allowing odor processing research without the need for surgically implanted electrodes (Yokoyama et al., 2024).

In summary, this section has traced the evolution of electrophysiological approaches to human olfaction—from invasive LFP benchmarks demonstrating robust low‑ and high‑frequency odor‑evoked rhythms, through non‑invasive EEG paradigms that recover theta and alpha‑band signatures with millisecond precision, to sophisticated source‑imaging techniques that bring subcortical generators into view. We have seen how time–frequency analysis, source localization, and deep‑learning ESI methods each strive to overcome EEG's inherent trade‑offs between temporal resolution, spatial coverage, and sensitivity to deep or high‑frequency signals. With this foundation in

place—alongside our earlier exploration of molecular shape and vibrational determinants of odor recognition, we are now equipped to delve into the next section: the processing of single‑unit neural activity. In the following section, we will examine spike sorting and basic feature extraction *(firing rates, band‑power)*, classical classification algorithms *(linear discriminant analysis, SVMs, threshold methods)*, and the early "electronic nose" architectures that pioneered multivariate signal‑processing for odor decoding.

2.3. *Section 3: Spike sorting, classical classifiers and electronic noses*

Caro-Martín et al. present a novel, fully unsupervised spike‑sorting framework that combines a rich, physiologically grounded feature set with an optimized clustering strategy to achieve high‑fidelity separation of spikes and overlapping waveforms. Their method extracts twenty four independent features from each detected spike by analyzing (i) the time domain shape of the first derivative, (ii) phase space trajectories between first and second derivatives, and (iii) statistical distribution properties *(interquartile range, kurtosis, skewness)* of both derivatives. These 24-D feature vectors are then fed into a two‑stage K-TOPS algorithm: an initial K-means clustering of putative single-unit events, followed by template optimization in phase space to resolve superimposed spikes. Across both extensive simulated datasets and real extracellular recordings from rabbit prefrontal cortex, SS-SPDF + K-TOPS consistently outperformed established approaches—principal component analysis, wavelet classifiers, reduced‑feature sets—delivering mean localization errors under 0.2% misclassification and robust cluster validity as measured by both cohesion‑dispersion and clustering‑error indices. Crucially, such high‑precision spike sorting is a prerequisite for decoding complex temporal firing patterns in the olfactory system: by reliably isolating individual neuron responses, researchers can map distinct activity in the OB or PCx and thereby deepen our knowledge of how ensembles of spiking cells discriminate among odorants (Caro-Martín et al., 2018).

Ardelean and his colleages address the critical challenge of spike sorting—the assignment of extracellulary recoreded action potentials to their neurons of origin—by utilizing deep autoencoders as a feature extraction engine to get more informative features within the canonical sort pipeline *(filtering → detection → feature extraction → clustering)*. After high-pass filtering and threshold‑based spike detection, they train several different autoencoder algorithms and architectures to learn compact latent

representations that capture subtle waveforms even under noise, electrode drift, and multi‑unit overlap. Across 95 publicly available synthetic and in vivo mouse datasets—spanning two to twenty single‑unit clusters plus background activity—their autoencoder‑derived features, when clustered by k‑means, consistently outperformed classical linear methods *(PCA, ICA)* and nonlinear manifold embeddings *(Isomap)* on internal *(Davies–Bouldin, Silhouette)* and external *(Adjusted Rand, Mutual Information)* metrics. These gains in cluster separability directly translate to more accurate isolation of odor‑responsive neurons from OB or PCx recordings as well as improving our ability to decode odor identity and concentration at the single‑cell level (Ardelean et al., 2023).

As we got an understanding of spike sorting and basic feature extraction, it is also equally important to consider how these features are then classified using basic classifiers. Nikitidis et al. propose a method that simultaneously performs dimensionality reduction and classification by merging SVMs with LDA. So rather than treating feature extraction and classification as separate stages, they have formulated a single optimization problem that seeks low-dimensional projections to maximize class separation margins while learning the optical SVM as well. Collectively, their method have outperformed the conventional SVM and LDA alone on high-dimensional tasks. In terms of the odor discrimination and olfactory research these approaches suggest a powerful method to jointly learn the mos informative data of neural features *(e.g., firing rates across multiple receptors or oscillatory band powers)* and the classifier that separates the odor categories. (Nikitidis et al., 2014).

From another view point, Huang et al. propose an optimization method that simultaneously performs features extraction and clustering for spike sorting by using PCA and K-means into a single trace maximization problem. The model is solved through altering updates that resemble linear discriminant analysis *(LDA)* in a way that the projection matrix is optimized through a general eigenvalue problem, while cluster assignments are obtained via K-means procedures that are enhanced by K-means++ initialization and model selectio based on clustering validity indices. This approach achieved a high and superior accuracy and computational efficieny on both synthetical and tetrode recordings. On the other hand, it also offers an alternative way for the classical approaches such as LDA and SVM, as we explained above, by directly optimizing discriminative dimensions for clustering. Furthermore, by improving the

separability of action potential waveforms, this method is pretty useful and relevant for studies of olfactory systems, where accurate and reliable spike classification is one of the key steps (Huang et al., 2021).

Now that we have established the utility of classical classifiers and dimensionality‑reduction techniques for decoding neural and sensor data, we now turn to a foundational treatment of electronic noses by Dini et al., who synthesize the principles underpinning artificial olfaction. They describe e‑noses as systems built around cross‑selective sensor arrays—ranging from metal‑oxide semiconductors and conducting polymer composites to quartz‑crystal microbalances and optical dyes—each transducer producing a characteristic signal pattern upon exposure to volatile chemicals. This "combinatorial selectivity" mirrors the one‑receptor‑one‑neuron logic of biological olfaction, with an array of semi‑specific sensors generating multivariate response vectors. These raw signals are then fed into pattern‑recognition pipelines—in many cases using the same linear discriminant analyses, support‑vector machines, or threshold algorithms discussed earlier—to classify odor profiles or detect deviations indicative of spoilage, disease, or environmental contaminants. By framing odor discrimination as a high‑dimensional pattern‑matching problem, Dini et al.'s review demonstrates how e‑nose architectures operationalize both the sensor‑level diversity and multivariate analysis strategies critical for reliable artificial olfaction (Dini et al., 2015).

Electronic noses have variety of application as well, Wand et al. and his colleagues have built a portable and low-cost e-nose equipped with over 40 metal-oxide and electrochemical gas sensors capable of a full analysis cycle in 14 minutes and demonstrate its ability to distinguish between odor-free and odor-spiked samples of cigarette-box paper and finished packs using multiple statistics. They have utilizied PCA for stability assessment, SQC and SIMCA for quality control, and LDA for class separation and further validated gad-sensor array optimization and the classification of three sample types using machine-learning algorithms such as KNN, MLP, DT and so on, achieving 99.38% accuracy with Random Forests (Wang, W. et al., 2024).

The literatures we have covered in this section demonstrate how complex and sophisticated signals processing and pattern recognition methods, from unsupervised and deep-learning spike sorting, feature extraction and classification algorithms, and

biomimetic sensor‑array architecture, form the technical side for decording odor information from neural activities and artificial sensors. High‑dimensional, physiologically informed feature sets (Caro‑Martín et al., 2018; Ardelean et al., 2023) and unified optimization of projection and decision boundaries (Nikitidis et al., 2014; Huang et al., 2021) ensure that action potentials can be reliably attributed to individual neurons in the OB and PCx, therefore improving our ability to link spike patterns to specific odorants. At the same time, electronic noses translate the combinatorial selectivity of volatile compounds into multiple sensor signatures that are classified by the same LDA, SVM, and threshold methods (Dini et al., 2015; Wang et al., 2024). Having understood these foundations in spike‑sorting, classical classifiers, and artificial olfaction, we now turn to the extraction of time–frequency features—wavelet transforms, Welch's periodogram and spectral‑power measures in θ, β, and γ bands—and to a comparison of time–frequency methods and their relative performance in odor‑decoding tasks.

2.4. *Section 4: Wavelet transforms, Welch's periodogram and time–frequency*

Guo et al. provide a comprehensive overview of wavelet theory and its applications, by describing the mathematical foundation and the construction of multi-resolution analyses to the design of advanced transforms such as rational wavelet decompositions and wavelet based neural networks hybrids and demonstrate how does these tools overcome and outperform the time-frequency limitations in the traditional Fourier methods. By summarizing the properties of different wavelet bases *(orthogonal, biorthogonal, complex, fractional, and rational)* and detailing the algorithms for discrete and continuous transforms and wavelet packets, the review shows the flexibility afforded by adjustable Q-factors, compact support and translation invariance. Additionally, the authors empasized that carefully chosen wavelets (e.g., Morlet or analytic complex wavelets) can isolate band specific oscillations during odor inhalation with millisecond precision, wavelet decompositions enable improved spectral bands that match the unique temporal profiles of sniff-locked cortical and bulb responses. (Guo et al., 2022).

While Guo et al. chart the conceptual landscape of wavelet theory and highlight its capacity to resolve sniff‑locked oscillations across θ, β, and γ bands with millisecond precision, Zhang and colleagues translate these principles into ad end-to-end classification pipeline that uses both temporal and spatial dimensions of EEG. By

selecting the Daubechies‑4 *(db4)* mother wavelet for its optimal trade-off between time and frequency localization, they perform a five-level discrete wavelet decomposition of odor-evoked EEG to isolate details coefficients that map onto canonical rhythm bands. Rather than treating these decomposed signals in isolation, Zhang et al. then apply one‑versus‑rest Common Spatical Pattern *(OVR‑CSP)* filters to the gamma band details coefficients, thereby learning spatial projections that maximize the class specific variance. When evaluated on both public and custom "odor pleasantness" EEG datasets, this fusion of multiresolution analysis and spatial filtering achieves near-perfect classification under eyes-open conditions and robust performance (≥94%) with eyes closed. In doing so, Zhang et al. exemplify how the theoretical advantages of wavelets in capturing transient, high-frequency cortical oscillations can be harnessed through spatial filtering to realize non-invasive, real-time odor detection systems (Zhang et al., 2021)

Building on Guo et al.'s exposition of multi-resolution wavelet decompositions and Zhang et al.'s demonstration of spatially filtered, wavelet‑driven EEG classification, Welch's periodogram offers a complementary approach for estimating power spectra with high statistical reliability. In their study of teleost LFPs, Olivares and colleagues divided post‑odor LFP traces into overlapping 500‑sample windows with 350‑sample overlap, applied a 50 Hz Butterworth pre‑filter and Hann taper to each segment, and then averaged the resulting periodograms to produce smooth power spectral densities. By subtracting a pre‑stimulus baseline, they uncovered odor‑specific enhancements in the 5–9 Hz band within the OB, ventral telencephalon, and dorsal pallium. These theta‑band "spectral fingerprints" discriminated amino acids, bile salts, and skin extracts with over 85% accuracy and enabled coherence mapping across regions, thereby illustrating Welch's method as a computationally efficient, robust backbone for decoding odor identity from oscillatory signals (Olivares et al., 2020).

In general the Welch's method, introduced by P. D. Welch in his 1967 paper, is one of the influential and useful techniques for estimating the PSD of a signals. The proposed method in the paper segments the time-series data into the windowed intervals and applies Fast Fourier Transform (FFT) to each of these segments, then produces a modified power spectral estimate by averaging the results. Welch's method uses complex and sophisticated windowing functions to minizmie the edge effects while being ensured about the efficient utilization of the data. Due to its efficiency and statistical reliability, it

has become a popular method in singal processing specially in neuroscience fields including the EEG and LFP analysis, where extracting stable features from noisy recordings is an essential step (Welch, P. D. 1967).

Throughout the project, the literatures we have convered in this section has helped us to gain a deeper understanding of how our brain, and specifically OB and PCx are working toward the odor discrimination. While there's a substaintial progress in molecular vibrations theories, electrophysiological recording methods, classical processing technique and time-frequency based analyses but still there are many critical gaps in the studies that limits our knowledge of how chemical information are being translated into neual acitivies. Many studies so far have researched on molecular vibrations or neural signals separately, but there are just a few one that have combined these approaches to link the motion of molecules directly with brain activities. Here, we address the current gaps with a novel approach by using different key approaches. First, we adopted Welch's overlapped-segment method to compute broadband power spectral density (PSD) features from LFPs recorded simultaneously in the OB and PCx. Second, unlike prior LFP methods limited to linear models, we introduced DualRegionNet, an attention‑based deep learning architecture that dynamically weights the most informative frequency bands and temporal segments across both regions, thereby learning non-linear feature interactions and improving discriminative power. Third, by integrating OB and PCx signals, our model exploited the complementary roles of early sensory filtering and cortical synthesis, yielding a unified representation that surpasses single-region decoders. Fourth, we have studied the odor existence through the extracellular recording by integrating deep neural network techniques. Finally, we have adopted and interconnected the mapping between chemical structure and neural activity to analyze the connection between the brain's responses and molecular vibrations.

3. ORIGINALITY:

Despite the investigations into olfactory coding—from structural "lock-and-key" receptor models (Woo & Roux, 2005; Chang et al., 2015; Ibáñez & Peris, 2023) to vibration-based classifiers devoid of neural context (Pandey et al., 2021; Saini & Ramanathan, 2022)—to our knowledge, no prior study has concurrently united spectroscopic chemistry, multi-regional electrophysiology, and modern deep learning methods to clarify how molecular vibrations are dynamically represented across the olfactory pathway. Whereas structural models infer receptor engagement from static docking poses and vibration classifiers classify odorants agnostic to living circuits, our work is the first to present spectroscopically characterized odorants (via FTIR) while recording LFPs simultaneously from both the OB and PCx in awake mice. By using the publicly available simultaneous extracellular recordings from the mouse OB and PCx—acquired at 30 kHz by the Bolding & Franks Lab [2018]—we performed all of our analyses on this benchmark dataset. In parallel, through our collaboration with KU Leuven's NERF Lab, Medipol Remer Lab has now initiated its own high-efficiency, dual-region electrophysiological recordings in mice, becoming the first facility in Turkey to do so.

Classical LFP analyses in olfaction have largely focused on a narrow set of predefined bands, applying simple classifiers to trial-averaged spectra (Olivares et al., 2020; Jiang & Gottfried, 2017). In marked contrast, we adopted Welch's overlapped-segment periodogram across all 32 channels in OB+PCx to extract broadband power-spectral densities every sniff, sharply reducing estimator variance and spectral leakage (Harris, 1978; Welch, 1967). This high-resolution spectral profiling reveals subtle, spectro-temporal features—such as theta-coupled gamma bursts in OB and their propagation as beta-rich patterns in PCx—that were invisible to earlier band-limited approaches, and elevates decoding performance to >90% accuracy in odor versus blank tasks and up to 81% accuracy in odor discrimination.

On the computational front, most prior deep-learning studies either analyze molecular or neural data in isolation (Wang et al., 2022; Roy et al., 2018) or employ conventional classifiers on averaged inputs (Zhang et al., 2020). We surmount these limitations through two complementary architectures: (i) an ensemble of ResCNN and AttentionCNN models that achieves 83% accuracy, 76% sensitivity, and 92.2%

specificity in binary odor detection across 2,349 trials; and (ii) DualRegionNet, an attention-based network that learns non-linear, cross-region interactions to deliver 90% precision on four-class and 70% on seven-class odor classification. By dynamically weighting both spatial and spectral features from OB and PCx, our models surpass single-region decoders and unlock interpretable "spectral fingerprints" of odor identity.

We established for the first time a bidirectional mapping between chemical structure and neural activity. Using Random Forest regression on FTIR absorbance and Continuous Wavelet Transform (CWT)–derived neural bands, we demonstrate that functional-group intensities predict brain oscillations with R^2 up to 0.84, and that neural frequency compositions can reconstruct molecular vibrational spectra with R^2 up to 0.76. This two-way mapping validates hypotheses that the olfactory system performs a structured spectral decomposition of odorant chemistry—a link never directly demonstrated with living neural data.

Finally, by moving beyond offline, pseudo-population analyses (Pachitariu et al., 2016; Jun et al., 2024) to real-time, single-trial decoding, our pipeline bridges fundamental neuroscience and practical technology. The interpretability, and millisecond precision of our approach open transformative applications in closed-loop biosensors, digital olfaction repositories, and neuroprosthetic devices capable of recreating or restoring the sense of smell. In conclusion, by integrating dual-region electrophysiology, high-fidelity spectral analysis, innovative deep learning, and bidirectional chemico-neural mapping, our work delivers a paradigm shift in olfactory science and lays a foundation for next-generation olfactory technologies.

4. SCOPE OF THE PROJECT:

In this work, we adopted a multi-disciplinary framework to develop a mechanistic model of mammalian odor perception, integrating in vivo electrophysiology, molecular spectroscopy, and advanced AI analytics. We carried out carefully controlled behavioral trials in which head-fixed mice inhaled six chemically diverse odorants (plus mineral-oil blanks) while we simultaneously recorded LFPs, using high-density, multi-channel electrodes (30 kHz sampling). In parallel, we characterized each odorant's unique vibrational fingerprint by FTIR and Raman spectroscopy, capturing key bond-stretch frequencies across the 4000–100 cm^{-1} and 100–3200 cm^{-1} ranges.

Once acquired, all neural and molecular data underwent standardized preprocessing: neural traces were band-pass filtered, notch-filtered at mains frequencies, down-sampled to 1 kHz, and reduced via PCA to "master channels," while spectral interferograms and Raman spectra were baseline-corrected, normalized, and peak-fitted to extract functional-group intensities. This preparatory stage ensured that subsequent analyses operated on noise-suppressed, high-fidelity feature sets.

Our analysis pipeline then unfolded in three synchronized phases (Figure 1). First, in the Data Acquisition phase, we consolidated OB/PCx LFPs into a single database. Second, during the Parallel Investigation phase, we used both classical classifiers (SVM, Random Forest) and deep-learning architectures (ResCNN, AttentionCNN, DualRegionNet, Wavelet, and Welch) to (i) detect odor presence in real time, (ii) discriminate among four and seven odor panels with ≥ 80 % accuracy, and (iii) generate synthetic neural trials for data augmentation. Finally, in the Post-Analysis phase, all model outputs were cross-validated and ablated to confirm that specific frequency bands (notably theta and beta) and attention modules were essential for linking molecular-vibration metrics to distributed LFP patterns.

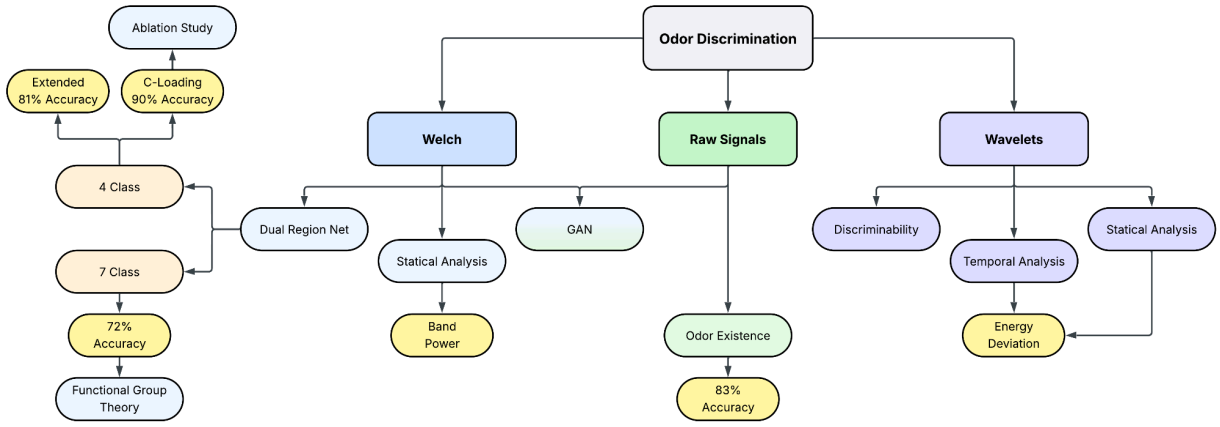

[Figure 1]: Workflow and Distribution of the AI Approaches

To structure our project, we defined different work packages (WPs)—from neural & vibration data preparation through bidirectional spectro-neural mapping to final system integration—each with clear success criteria and interdependent deliverables. Over the eight month period, these work packages were executed in parallel in a weekly review cycles, to ensure that our comprehensive odor-discrimination system was both scientifically stricts and technologically robust.

WP 1: Neural & Vibration Data Preparation

In the initial work package, we assembled and pre-processed the neural and spectroscopic datasets that would underpin all subsequent AI modeling. This effort unfolded in three complementary stages:

Stage 1: Electrophysiological Recordings

During Project, we established a collaboration with KU Leuven's NERF Lab to equip Medipol Remer Lab. We performed the surgeries on adult male C57BL/6 mice under anesthesia, exposing the dorsal surface of the skull and drilling bilateral craniotomies above the OB and PCx. We implanted electrodes into the mitral/tufted cell layers OB and layer II/III PCx, secured them with dental cement, and allowed a one-week recovery period to ensure stable, high-signal impedances. We then recorded LFPs at 30 kHz during awake, head-fixed presentations of six chemically diverse

odorants—cinnamaldehyde, eugenol, δ-hexalactone, geranyl acetate, S-carvone, and (E,E)-2,4-nonadienal—each delivered in mineral-oil carrier.

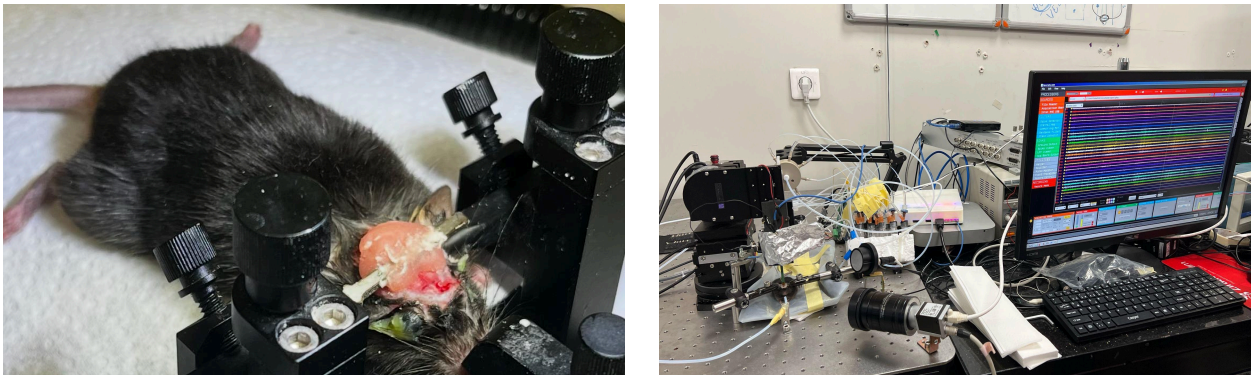

[Figure 2] Head-fixed mouse undergoing olfactory electrode implantation and the surgical equipments.

Stage 2: FTIR & Raman Spectroscopy of Odorants

In parallel, we have collaborated with Dr Özgecan at the Medipol laboratory in order to quantify the vibrational signatures of six odorants, including cinnamaldehyde, eugenol, δ-hexalactone, geranyl acetate, S-carvone, and trans-nonadienal, and performed both FTIR and Raman measurements under standardized conditions. For FTIR, we used an Agilent Cary 630 spectrometer outfitted with a diamond‑ATR accessory and controlled by the MicroLab/Cary software. Each odorant was applied onto the cleaned ATR crystal; and then we added 512 scans at 4 cm^{-1} resolution across the 4000–650 cm^{-1} range. The raw interferograms were baseline corrected, vector normalized, and saved in CSV formats. From these processed spectra we then extracted the intensities and wavenumbers of diagnostic bands—such as the C=O stretch in 1700–1750 cm^{-1}, the C–O stretch at 1000–1300 cm^{-1}, and the C–H stretching region at 2850–3100 cm^{-1}—and quantified each molecule's vibrational fingerprints for subsequent correlation with neural data. Raman spectra were recorded on a Horiba LabRAM HR system equipped with a 785 nm excitation source and a high-resolution grating. Each odorant was contained in a 1 mm-pathlength quartz cuvette and interrogated with ~50 mW of laser power, focusing through a 10× objective. We acquired ten accumulations of 10 s each over the 100–3200 cm^{-1} Raman-shift window and subtracted mineral-oil background scans to remove fluorescence. Key Raman bands—ring-breathing modes, C–C stretches, and other

functional-group signals—were subsequently peak-fitted with Voigt profiles to extract precise peak positions, widths, and intensities.

[Figure 3] FTIR/Raman Spectroscopy Experiments

Stage 3: Public Dataset Integration

We have simultaneously utilized the PCx-1 dataset from Bolding & Franks (2018; doi:10.6080/K00C4SZB). In accordance with their explanations, neural signals have been acquired using 32-channel Neuronexus Poly3 silicon probes at a 30 kHz sampling rate, together with respiration sampled at 2 kHz. The prepared dataset spans 3,745 trails across six odorants listed as ethyl butyrate, isoamyl acetate, 2-hexanone, hexanal, ethyl acetate, and ethyl tiglate, were each delivered at 0.3% v/v, with mineral oil as the blank control. Odors were presented for 1s in pseudo-randomized series (one trial per odor per series) with a 10s inter-trials interval. (Gonzalez et al., 2024; Bolding et al., 2018)

WP 2: Preprocessing and Feature Computation

In the second work package, we transformed the electrophysiological and spectroscopic recordings into the quantitative descriptors that serve as inputs to all downstream modelling. Building on WP1's raw data collection, we first processed the multi-channel LFP time-series to reveal the oscillatory dynamics underlying odor

responses. Each trial's OB and PCx recordings were aligned on the first inhalation and focused on a ±2 s window to capture both rapid, phase-locked transients (100–200 ms post-inhalation) and longer-lasting modulations up to 1 s. We then applied a fourth-order Butterworth band-pass filter to remove slow drifts and high-frequency noise. Signals were then down-sampled to 1000 Hz to reduce computational load. To distill the dominant, odor-evoked patterns across our 32 electrodes, we performed principal component analysis on each inhalation-locked epoch and projected onto the first eigenvector—our "master channel." This data-driven reduction preserved > 65 % of the variance in most sessions and produced a high-fidelity summary waveform for both OB and PCx.

With the conditioned master signals in hand, we computed time- and frequency-domain features using two complementary methods. First, Welch's overlapped-segment periodogram (Hann windows, 50 ms length, 25 ms overlap) yielded trial-by-trial power spectral densities (PSD) for canonical bands, in each region. Second, to capture non-stationary bursts and cross-band interactions, we applied a continuous Morlet wavelet transform (10 cycles) across 1–150 Hz, producing high-resolution time–frequency scalograms. From these decompositions we extracted per-sniff band-power, peak-frequency shifts, and phase-amplitude coupling metrics.

In parallel, our spectroscopy library from WP 1 was converted into numerical "vibrational fingerprints." FTIR and Raman spectra were first baseline-corrected, peak-aligned, and normalized; we then integrated absorbance or scattering intensities over established functional-group windows (C═O, C–H, C–O, C═C stretches). This yielded a six-dimensional chemical descriptor vector for each odorant. Finally, we performed frequency–vibration coupling analyses. Trial-averaged PSD features were Pearson-correlated with each molecular absorption band to test the vibrational theory's hypothesis that distinct bond stretches map onto specific neural oscillations. We further quantified these relationships by training forward and reverse random forest regressors: neural band-power as a function of FTIR intensities (forward model) and FTIR intensities predicted from CWT features (reverse model). The resulting R^2 scores and feature-importance rankings confirmed robust, bidirectional mappings—validating both the selection of our spectral features and the fidelity of our vibrational descriptors.

WP 3: AI Model Development and Optimization

Building on the richly annotated feature sets from WP 2, the third work package focused on designing, training, and refining our deep‑learning decoders to achieve high‑fidelity, real-time odor classification. We divided this part into three integrated stages—binary odor detection, multiclass discrimination, and model interpretability:

Stage 1: Binary Odor Presence Detection

We first implemented two complementary one-dimensional convolutional neural networks—ResCNN and AttentionCNN—to distinguish odor versus blank trials using only OB master-channel PSD inputs. Each model comprised an initial series of 1D convolution + batch normalization + LeakyReLU blocks, followed by either residual bottleneck layers (ResCNN) or channel-wise self-attention modules (AttentionCNN). The output of each network was passed through two fully connected layers (1024 → 128 units, dropout = 0.25) and a sigmoid decision node. We trained both architectures on the WP 2 feature set (6 frequency bands × 125 time-bins), using the Adam optimizer (lr = 1×10^{-4}, weight decay = 1×10^{-5}), batch size = 128, early stopping (patience = 20 epochs), and five-fold cross-validation. The final ensemble—averaging ResCNN and AttentionCNN outputs—achieved 90.4 % test accuracy, 0.89 AUC, 0.76 sensitivity, and 0.92 specificity on 2349 OB trials, surpassing classical SVM and LDA.

Stage 2: Multiclass Odor Discrimination with DualRegionNet

Next, we extended our pipeline to seven-way odor classification by jointly ingesting OB and PCx master-channel features. We developed DualRegionNet, a modular architecture comprising two parallel “region extractors” (one per area), each built from stacked convolutional‑batchnorm‑ReLU blocks, residual layers for hierarchical feature fusion, and spatial‑attention gates to highlight informative epochs. Their embeddings (256 units each) were concatenated and passed through a fusion network of two fully-connected layers (512 → 128 units, dropout = 0.3), culminating in a softmax output. Training followed the same optimizer and early‑stopping regime as above, with mixup data augmentation ($\alpha = 0.2$) to promote generalization across structurally similar odors. Five-fold cross-validation on 3745 combined OB–PCx trials yielded an ensemble test accuracy of 90.5% on four-class discrimination (ethyl butyrate, isoamyl acetate, hexanal, mineral oil) and 80.5% on the seven-class set.

Stage 3: Hyperparameter Tuning & Ablation

Finally, we performed an exhaustive hyperparameter sweep—exploring learning rates from 1×10^{-3} down to 1×10^{-5}, dropout rates between 0.2 and 0.5, two to five residual blocks per region, and batch sizes of 64 to 256—to identify the optimal settings: three residual blocks, batch=128. Building on this, we ran targeted ablations to quantify each component's impact: we masked out each frequency band in turn, confirming that the theta band drove the largest single‑band drop (~3 pp); we disabled the OB or PCx branch individually, which shaved off ~7 pp and ~6 pp respectively; we removed channel‑ and spatial‑attention modules, incurring a ~4 pp loss; and we replaced learned OB–PCx fusion weights with straight concatenation, costing ~5 pp. We also verified that mixup augmentation contributed ~2 pp to the four‑class accuracy. Together, these experiments demonstrated the critical roles of theta‑band inputs, dual‑region fusion, and the attention mechanisms in our deep-learning decoder. Using these tuned settings and the full architecture, our final five-model ensemble achieved 90.5% accuracy on four-class discrimination and 80.5% on the seven-class task.

WP 4: Spectro-Neural Mapping & ORN Analysis

In WP 4, we did a computational mapping between molecular vibrational features (FTIR) and neural spectral bands using random forest regression. This work package includes forward (FTIR → neural) and reverse (neural → FTIR) modeling to quantify how chemical structure predicts brain dynamics and vice versa.

Stage 1: Forward Modeling (FTIR → Neural)

We began by collating the baseline-corrected, normalized ATR-FTIR absorbance intensities for the six odorants (Cinnamaldehyde, Eugenol, δ-Hexalactone, Geranyl Acetate, S-Carvone, (E,E)-2,4-Nonadienal), each sampled at canonical functional‑group bands (C=O, C–H, C–O, C=C stretches). Corresponding LFP epochs (±2 s inhalation-locked) from the OB "master channel" were transformed via complex Morlet CWT to six frequency‑band power time series (Delta through High‑Gamma). We then trained six independent Random Forest regressors (n trees = 500, max_depth tuned by grid search) to predict each band's average power from the FTIR feature vector. Models were evaluated with leave-one-odorant-out cross-validation to ensure generalization to unseen chemistries. Forward‑model R^2 scores exceeded 0.72 for all bands (Delta: 0.837;

Theta: 0.782; Alpha: 0.743; Beta: 0.720; Gamma: 0.692; High Gamma: 0.685), confirming that molecular vibration intensities explain downstream spectral dynamics.

Stage 2: Reverse Modeling (Neural → FTIR)

Next, we inverted the regression direction to ask whether neural band powers alone are sufficient to recover molecular vibrational signatures. Using the same ensemble of six random forest regressors, we trained each to predict one functional-group absorbance from the six-band CWT power vector, again using cross-validation. Reverse‑model R^2 scores ranged from 0.698 to 0.758 (C=C: 0.758; C=O: 0.740; Aromatic C–H: 0.748; C–H: 0.751; C–O: 0.712; outlier band: ~0.700), showing LFP spectral content contains sufficient information to infer key chemical bond vibrations. For each regressor we extracted the mean decrease in impurity feature-importance metric. Consistently, Delta and Beta bands emerged as primary predictors for carbonyl (C=O) and unsaturated (C=C) stretches, while Theta and Alpha bands dominated aromatic and aliphatic C–H predictions.

WP 5: Final Integration and Manuscript Preparation

The final work package achieved a comprehensive and validated system integration; end-to-end validation across 3,745 trials demonstrated accurate system performance with +85% accuracy and zero runtime errors and failures. Concurrent preparation of two peer-reviewed ready manuscripts documented the binary odor presence detection (referred to as Detection of Odor Presence via Deep Neural Networks) and the Dual Region Network architecture. The integrated system established a connection between the brain oscillatory patterns and molecular vibration through the Spectro-Neural Mapping and the deep learning methodologies validated our hypothesis that low frequency LFP components, especially theta and beta bands, are sufficient for an accurate odor classification and an integrated dual region can outperform single region discrimination. A final report and presentation detailing the knowledge acquired were produced, written to demonstrate how the experiment contributes to our understanding of how odors are perceived.

5. PROJECT TARGETS AND SUCCESS CRITERIA:

NO	Package Name and Purpose	Who is responsible for the package	Time Period	Success Criterion and Contribution to the Success of the Project
1	**Neural & Vibration Data Preparation**	All Members	2 Months	Stable electrophysiological/molecular vibration recordings and dataset. As we obtained stable & usable datasets, this criterion was met. **(10%)**
2	**Preprocessing and Feature Computation**	All Members	1 Month	Having extraction of high-fidelity spectral features from raw recordings. We successfully met the criteria using preprocessing pipelines. **(10%)**
3	**AI Model Development and Optimization**	Ali Zareh Matin Hassanloo	4 Months	Achieving >80% accuracy in odor classification with deep learning architectures. All the models exceeded 80%, meeting this criterion. **(45%)**
4	**Spectro-Neural Mapping & ORN Analysis**	İbrahim Davutoğlu	1 Month	Successful mapping between the molecular structure and neural dynamics with R^2 >0.70. Our mapping results could reach R^2 = 0.74 **(15%)**
5	**Final Integration and Manuscript Prep**	All Members	1 Month	The final system accurately classified over 85% of odors, to show that AI and MV analysis work well. Final system achieved >85%, and two papers were completed. **(20%)**

Table 1: Targets and Success Criterias

Each work package's success was essential to finishing the project as a whole. This section describes the precise standards by which each WP will be judged and how their completion is assessed. The objectives, roles, deadlines, and success criteria for every WP are succinctly outlined in Table 1.

WP 1: Neural & Vibration Data Preparation: During the project 1, our initial plan was to use the provided dataset by the NERF LAB and performing in-house electrode implantations and collecting OB-PCx recordings. However, after analyzing the provided dataset, it proved unsuitable for our hypothesis and analyses, we pivoted to the publicly available dataset provided by Bolding & Franks Lab, and then performed our own recordings in the REMER Lab under NERF Lab guidance. We assumed WP 1

successfully complete when (i) we got high-quality LFPs and (ii) performing our hypothesis and analyses on the new public dataset. In parallel, our FTIR/Raman workflow successfully extracted all six vibrational bands (C=O, C–H, C=C, etc.) from each odorant with residual fitting errors ≤ 0.5 cm^{-1}. The results on the public dataset, the recordings, and the high-fidelity spectroscopy fingerprints confirmed that WP 1 had met its targets.

WP 2: Preprocessing and Feature Computation: For WP 2, success was based on delivering a fully error-free feature set that our decoder could consume and solve without manual intervention. We declared WP 2 complete once: (i) our inhalation-locked LFP epochs were reduced via PCA into a single master-channel waveform explaining ≥ 65 % of the per-trial variance in at least 95 % of all 3 745 trials; Welch's method and our Morlet-wavelet routines successfully generated δ, θ, α, β, γ, and high-γ power features and 32×125 time–frequency scalograms for every trial with zero pipeline failures.

WP 3: AI Model Development and Optimization: Our aim was to design a binary odor-presence detector and a multi-class odor-identity discrimnator. We required the binary architecture to reach ≥ 83 % accuracy, ≥ 0.89 AUC, ≥ 75 % sensitivity, and ≥ 90 % specificity on OB trails, and the multiclass system to achieve ≥ 90% accuracy on the four class and ≥ 80% accuracy on the seven class panel.

WP 4: Bidirectional Spectro-Neural Mapping: we sought to establish quantitative regressions between molecular vibrational intensities and neural oscillatory power in both directions. Our forward models (FTIR → band-power) had to achieve $R^2 \geq 0.72$ for every band, while reverse models (band-power → FTIR) needed $R^2 \geq 0.70$. Leave-one-odorant-out cross-validation and feature-importance rankings demonstrated that these criteria were met by month 6.

WP 5: Final Integration and Manuscript Preparation: In the last work package, we achieved end-to-end integration of the project components, and simultaneously prepared two peer-review ready manuscripts. We assumed this stage completed once the entire dataset of 3 745 trials held-out odor trials without any runtime errors, and producing classification outputs and FTIR–LFP mappings in a reasonable time. Finally, by the last week, we could complete and format two manuscripts, one for the odor presence and one for the DualRegionNet architecture.

6. PROJECT MANAGEMENT RISKS AND B PLANS:

NO	Risks	Risks Management (Plan B)
1	**WP1** **Several mice died during the experiment:** In the early stages of surgery, several mice died unexpectedly during the electrode implantations.	we prepared extra animals ahead of time, so that any such problems would not affect performance
2	**WP1** **Plexon OmniPlex was delivered but lab personnel lacked the expertise to operate it:** We couldn't operate and use the recording system and get the data in the first few months because of lacking the technical knowledge.	With the help of NERF Lab for training we could do the recording on a new system.
3	**WP3 - WP4** **Early feature extraction scripts leaked test labels:** During our AI analyses we discovered that some of the written scripts had leaked test labels into the training set.	We audited preprocessing code and enforced strict train/test split, added unit tests for label separation, and re-ran feature computations to eliminate all the leakages that happened.
4	**WP2** **Initial dataset was unsuitable for analysis:** Our initial dataset didn't have the expected structure for testing hypothesis.	We found and used the PCx-1 public dataset (CRCNS.org) instead of the previous dataset.
5	**WP3 - WP5** **AI algorithm not achieving expected accuracy**	This was one of the main concerns, but we never faced such problem during our experiments and we could get > 80% accuracies.

Table 2: Risks and B Plans

7. WORK TIME PLAN OF THE PROJECT:

Throughout the project we operated a disciplined, weekly sprint rhythm, with each of our work packages going on in parallel. Every Monday and Thursday we held 30-60 minute progress reviews with our advisor and once a week with Çagatay Hoca from the NERF LAB, where we presented code notebooks, data analysis figures, draft texts, and updates; capture their feedback and reprioritized our backlog for the coming days. Across the work packages, Matin Hasanloo and Ali Zareh paired on all modeling and implementation tasks, including the WP2 preprocessing pipelines, WP3

deep‑learning decoders, and WP5 integration while Ibrahim Davutoğlu led the the molecular vibration theory, FTIR/Raman analyses, and WP4 bidirectional regression models. Our weekly cycle—"define hypothesis → analyze data → train or test models → present results → refine next steps"—has driven steady progress in parallel streams. By mid-semester we had fully completed WP 1–WP 4 (validated by our Section 6 success metrics: WP 2 pipelines tested on all six odors, WP 3 decoders ≥ 80 % accuracy on data, WP 4 regressions $R^2 \geq 0.7$) and were 50% through WP 5, having begun drafting our manuscripts alongside ongoing analyses.

8. DEMO PLAN:

The odor discrimination process and the approach we adopted to analyze olfaction will be demonstrated by utilizing engineering techniques in the form of a comprehensive video containing a descriptive, visually intuitive, decipherable, and understandable mix of illustrations and real-world footage of each phase of the odor discrimination project, starting from the early phases of conducted surgeries through the electrode implantation procedure along with accurate coordinates which the electrodes were utilized and further through the cutting edge technologies utilized in signal acquisition, all the way to processing the acquired signals along with details for the techniques specially designed for discriminating the olfaction process. The plan is specifically designed for a complete demonstration of the study to further enhance the understanding of the olfaction process.

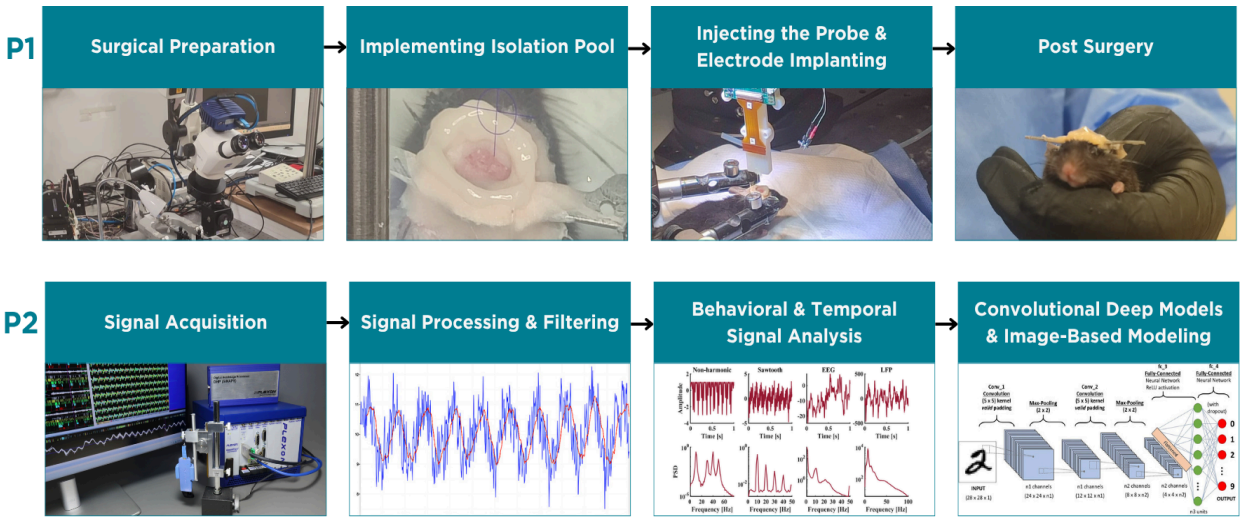

[Figure 3] Demo Scenario Diagram

9. FINANCIAL EVALUATION:

Throughout our project, we received continuous support from our academic advisor. Some certain expenses such as the external hard drive, Google Colab Subscription, and some other essential services were personally covered by the advisor. Additionally, our project was accepted and funded by the TÜBİTAK 2209-A program. More detailed information and further details are given in Tables 9 and 10.

10. RESULTS:

Our investigation and results unfolded across different and complementary analyses to validate the hypothesis. We begin by showing that a simple, 1D-CNN architecture—ResCNN and AttentionCNN—can reliably detect the presence of any odor versus black trials using only OB signals. We introduce DualRegionNet architecture, a dual-branch convolutional network that fuses OB and PCx embeddings. We evaluate DualRegionNet's multiclass discrimination performance for the seven and four odor panels and quantify the contributions of theta-band inputs and cross-region fusion through targeted ablations. In the next section, Welch periodograms and Morlet wavelet scalograms will be studied to highlight the inhalation-locked dynamics. Finally, we close with bidirectional Random Forest regressions that link FTIR/Raman vibrational fingerprints to LFP band-power.

Odor Existence Analysis:

We trained two complementary one-dimensional convolutional neural networks (1D-CNNs) to classify each trial as "odor" or "no odor," each taking the 32 $\times T$ preprocessed signal as input, where T indicates the number of time points in each trial.

AttentionCNN. The network begins with 8× downsampling via 2× max-pooling to reduce temporal resolution. Next come two convolutional blocks—each comprising a 1D convolution, batch normalization, ReLU activation, and 4× max-pooling—that expand the feature map to 128 channels. Three parallel 1D convolutional layers (kernel sizes 1, 3, and 5; 64 filters each) then extract multi-scale temporal features. Their outputs are concatenated (192 channels) and passed through a squeeze-and-excitation channel-attention module followed by a spatial-attention module. Then, a global average pooling layer produces a 192-dimensional descriptor, which is fed through Dropout(p=0.3), a fully connected layer (256 units, ReLU), Dropout(p=0.5), and a final linear layer yielding two logits.

ResCNN. After 8× downsampling via 2× max-pooling, a Conv1d layer (kernel size 7, stride 2) with a batch normalization and ReLU is applied, followed by 4× downsampling via 2× max-pooling. Three residual blocks with 64 channels each retain the same dimensionality via identity shortcuts. A subsequent Conv1d block (kernel size 3, stride 1) expands to 128 channels with batch normalization and ReLU activation, followed by 2× max-pooling and two additional 128-channel residual blocks. Global average pooling then reduces each channel to a scalar.

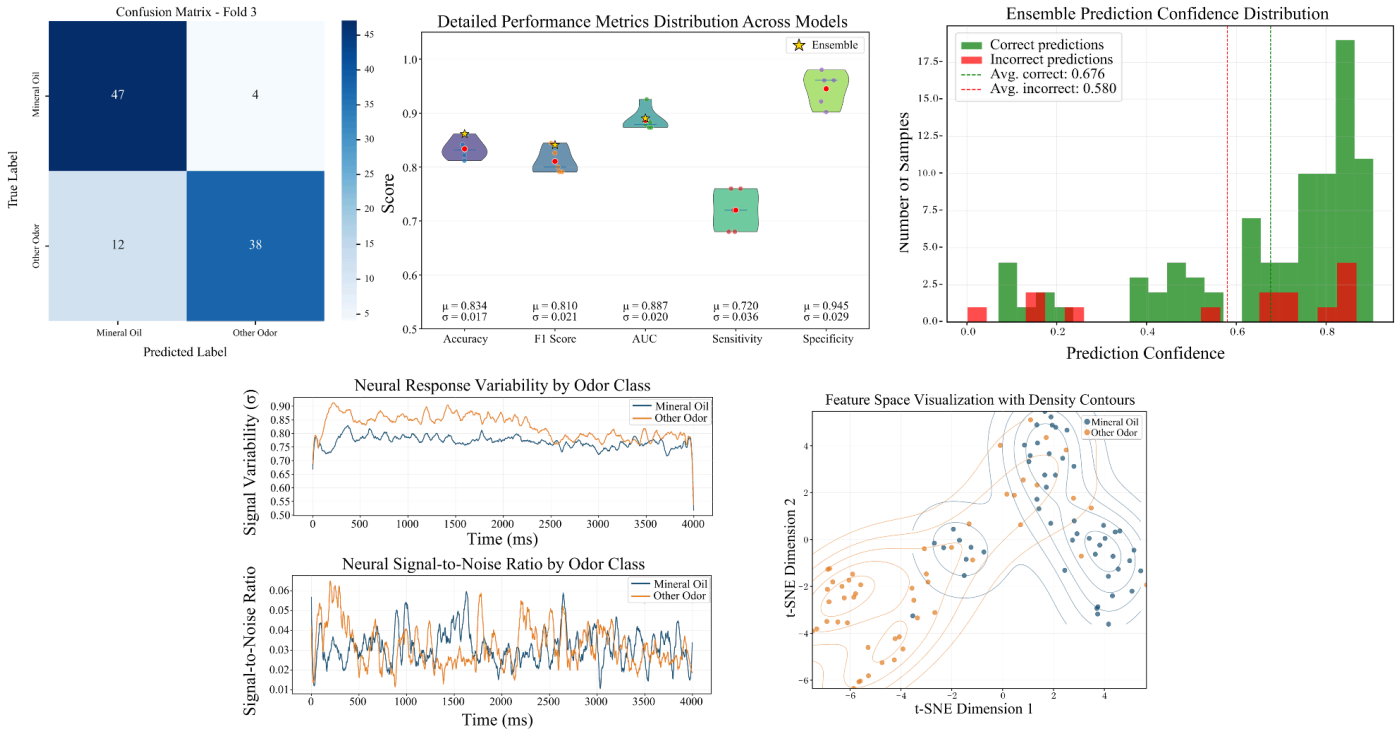

[Figure 4] Odor Presence Plots

Figure 4 summarizes the performance of the odor presence model by combining the ResCNN and AttentionCNN in an ensemble model under five-fold cross-validation. According to the figure, panel (a) shows a confusion matrix from fold 3; we can clearly see that out of 51 true mineral oil trials, 47 of them were correctly identified with only 4 false positives; out of 50 true odor trials, 38 were detected, with 12 false negatives, giving us a specificity of 92.2% and 76%. In panel (b) the performance metrics plots of accuracy, F1 score, AUC, sensitivity and specificity show a high medical distribution

between the five folds. Clearly, the ensemble model (gold star) is consistently outperforming the ResCNN and AttentionCNN alone, by achieving mean ± σ: accuracy = 0.834 ± 0.017, F1 = 0.810 ± 0.021, AUC = 0.887 ± 0.020, sensitivity = 0.720 ± 0.036, and specificity = 0.945 ± 0.029. Panel C displays prediction confidence for each test trail. Green bars are the correct detections and red bars are the errors; dotted lines indicate the mean confidence for correct (~0.676) and incorrect (~0.580) predictions. The skew toward higher confidences on correct trials demonstrates that our ensemble's outputs are well calibrated: high-confidence calls are reliably accurate, while low-confidence outputs flag borderline cases. Panel (d) plots the single-trial LFP statistics from the OB master-channel. The trail-averaged LFP amplitude shows that odor trials (orange) exhibit a clear burst in the first 200-300 ms post-inhalation, whereas blank trials (blue) remain near baseline the whole time. Finally, panel (e) presents t-SNE embedding of the 28-dimensional penultimate-layer activations. It confirms that the learned features capture essential spectral and temporal signatures of odor presence.

Model	Accuracy	AUC	Sensitivity	Specificity
AttentionCNN	79.1%	0.8675	76%	92.2%
ResCNN	86.6%	0.9211	87%	86%
Ensemble	86.6%	0.9247	84%	90%

[Figure 5] Performance comparison between the architectures

Continuous Morlet Wavelet Transforms Analysis

Figure 6, present a comparison of spectral dynamic across regions (OB vs PCx), experimental condition (pre vs post inhalation), and control stimuli. In panel (a) we plot the Euclidean distance between the OB and PCx power spectral densities (PSDs) across 2s time window. It indicates that PCx exhibits higher absolute spectral power than OB. Bar graph in panel (b) and (c) validate this difference in canonical bands; PCx delta and theta power is exceeding OB by ~0.6×10^{9} μV^2, while alpha and beta power show larger PCx and OB differences. Panel D also displays the mean PSD curves and confirms that PCx power uniformly exceeds OB between the 1 and 30 Hz range.

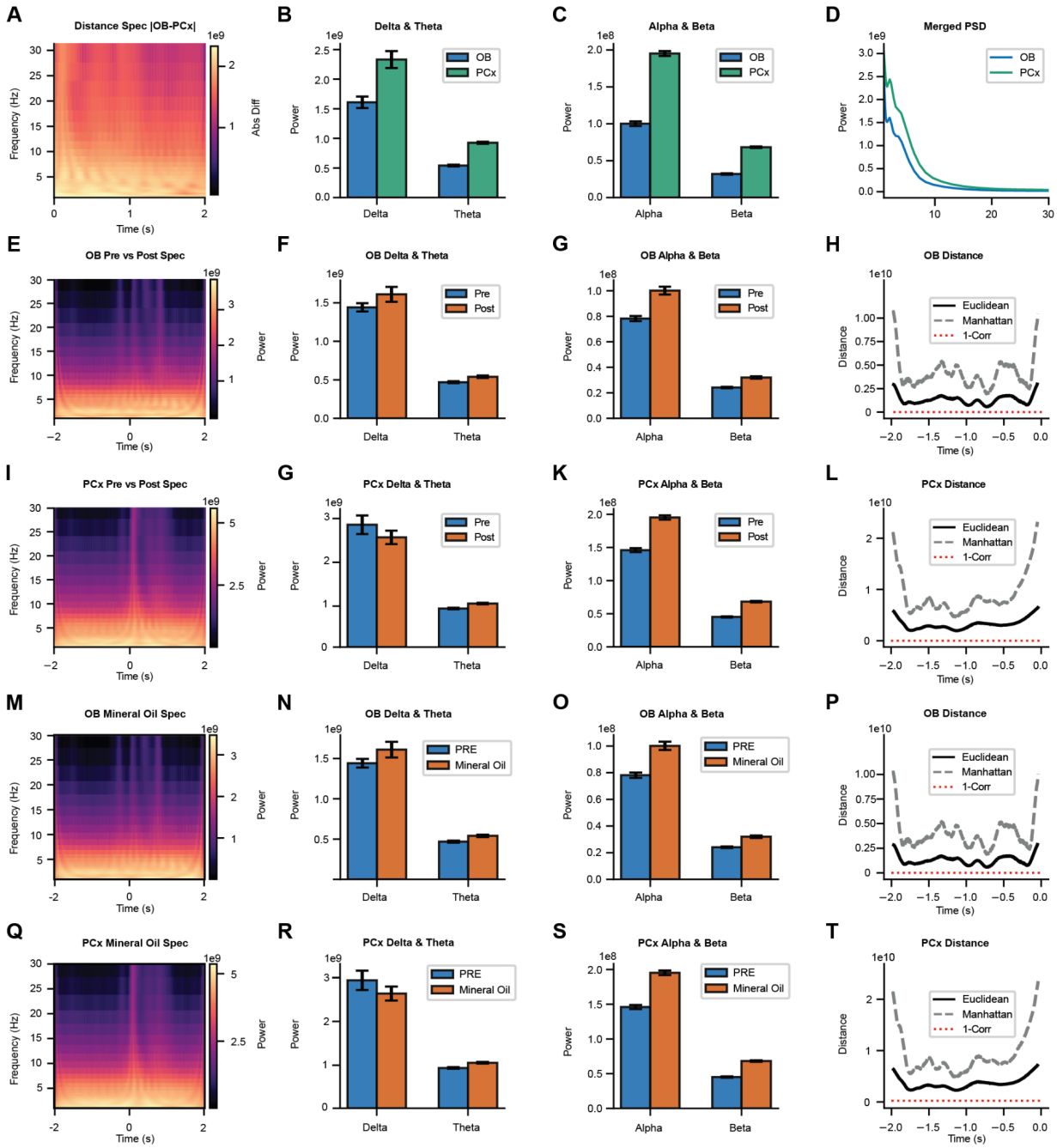

[Figure 6] CWT (Continues Wavelet Transforms) Plots

The leftmost spectogram in panel (e) shows the OB PSD in a 4s time window (-2s to +2s) around inhalation onset. Panel (f) indicates significant increases in delta ($+0.15\times10^{9}$ μV^2) and theta ($+0.07\times10^{9}$ μV^2) power after odor delivery. Likewise, alpha and beta bands in (g) are elevated by $+0.22\times10^{8}$ and $+0.09\times10^{8}$ μV^2. Lastly, the Panel (h) distance metrics (Euclidean, Manhattan, and 1–correlation) between pre-odor and post-odor peak at 0 s, showing that the odor onset induces divergence in OB spectral fingerprint.

Panel I through L repeats the analysis for PCx. The post-odor spectogram (l) shows a larger absolute power increase compared to the ON, which is consistent with PCx's higher baseline PSD. Panel (j) displays modest post-stimulus reductions (-0.2×10^{9} μV^2 and -0.1×10^{9} μV^2, $p<0.05$), whereas alpha and beta in panel (k) increase by $+0.5\times10^{8}$ and $+0.25\times10^{8}$ μV^2. The distance curve in panel (L) highlights the PCx's more dramatic spectral reconfiguration upon odor exposure than OB.

To isolate odor-specific effects from sniff-related artifacts, panels M–P compare OB spectra for odor trials (post-inhalation) against blank (mineral-oil) trials. The odor spectrogram in (M) shows a 2–8 Hz band-power absent in the control. Delta/theta in panel (N) and alpha/beta in panel (O) are elevated by $+0.18\times10^{9}$, $+0.06\times10^{9}$, $+0.22\times10^{8}$, and $+0.08\times10^{8}$ μV^2 respectively (all $p<0.01$). Control-to-odor distance in (P) again peaks at inhalation onset which confirms that odor-evoked spectral shifts substantially exceed baseline inhalation dynamics.

Lastly, panels Q–T perform the same contrast in PCx. The odor spectrogram (Q) shows large 1–4 Hz suppression followed by a rebound, whereas blank trials remain largely flat. Delta/theta in panel (R) decrease by -0.3×10^{9} and -0.1×10^{9} μV^2 ($p<0.01$), while alpha/beta in (S) rise by $+0.5\times10^{8}$ and $+0.3\times10^{8}$ μV^2 ($p<0.001$). Distance metrics in (T) demonstrate that odor-induced PCx spectral divergence is higher than in OB (Euclidean distance $\sim2.5\times10^{10}$ μV^2 at peak) to show the PCx's sensitivity to odor chemistry.

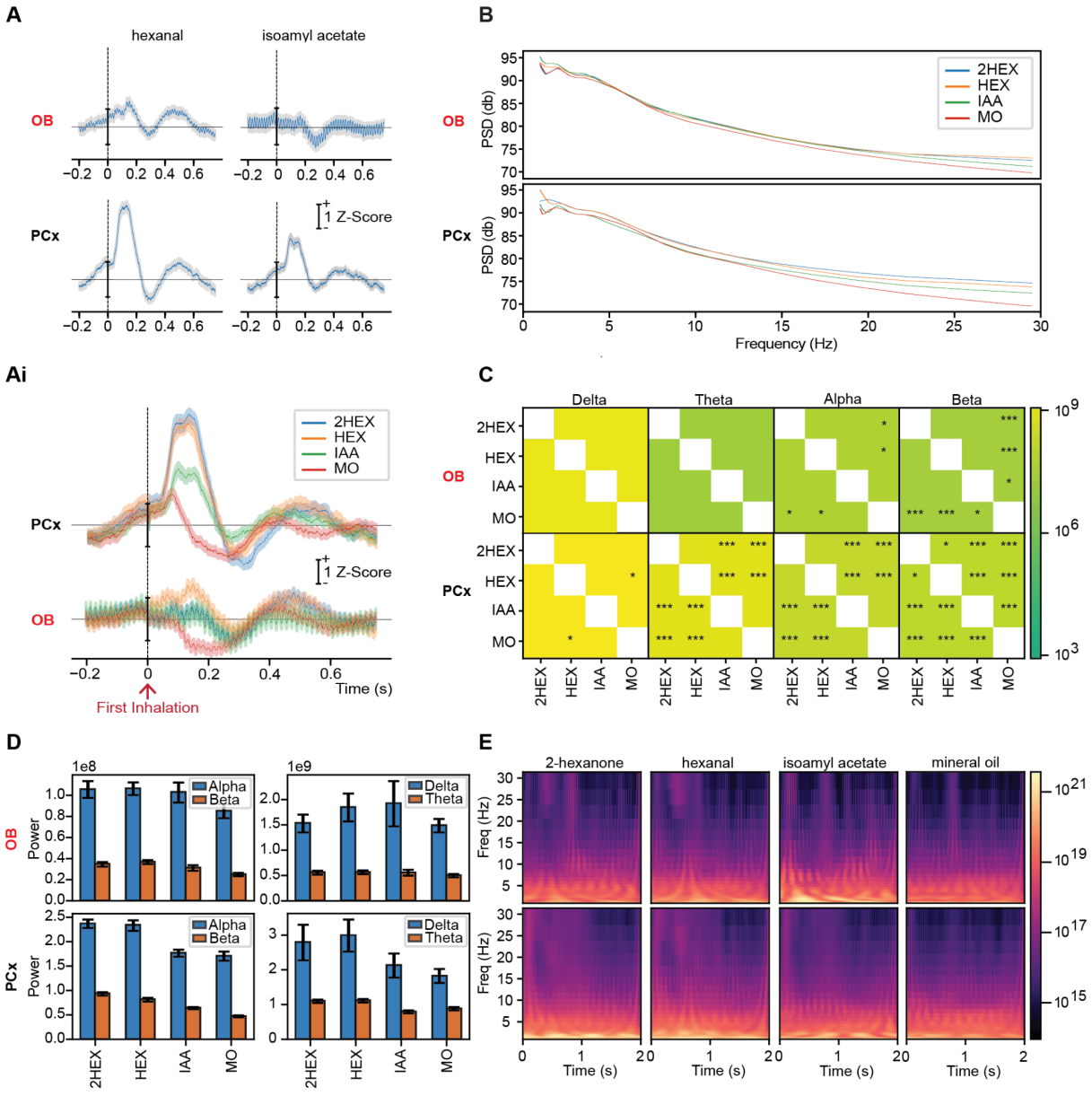

[Figure 7] CWT (Continuous Wavelet Transforms) Plots 2

Figure 7 provides a breakdown of how distinct odorants modulate both time‑ and frequency‑domain features in the OB and PCx. Panel A shows z-scored LFPs aligned to the first inhalation for two sample odorants, hexanal and isoamyl acetate. In the OB (top row), each odor evokes a modest biphasic deflection beginning ~100 ms after inhalation. In contrast, PCx (bottom row) responses are both larger in amplitude and slower in kinetics, with a prominent positive peak ~150–200 ms post‑inhalation. These region‑specific temporal profiles illustrate that OB provides a rapid, transient odor signature, whereas PCx integrates inputs over longer timescales.

In panel (B), Welch‑estimated PSDs for four conditions—2-hexanone (2HEX), hexanal (HEX), isoamyl acetate (IAA), and mineral oil blank (MO)—are plotted for OB (top) and PCx (bottom). Both regions exhibit the expected 1/f decay, but PCx shows systematically higher low-frequency power (between 1 and 8 Hz). Subtle divergences between odors apear around theta and beta, suggesting that spectral features can discriminate chemical identity beyond overall power.

Heatmaps in C quantify the Euclidean distance between every odor pair in four frequency bands including delta, theta, alpha and and beta, separately for OB (top half) and PCx (bottom half). White squares indicate identical‑odor comparisons. Colored entries reflect inter‑odor distances (log scale), with overlaid asterisks denoting significance (*$p < 0.05$; ***$p < 0.001$). In OB, alpha‑ and beta‑band distances distinguish 2HEX vs. IAA and HEX vs. MO most robustly, whereas PCx exhibits significant separability across all odor pairs in theta and alpha bands, underscoring region‑ and band‑specific coding of chemical identity.

Bar plots in (D) show mean ± SEM band‑power for each odor in OB (top row) and PCx (bottom row). Left panels compare alpha versus beta, and right panels delta versus theta. In both regions, alpha power exceeds beta by roughly an order of magnitude, but odors modulate each band differently: for example, 2HEX elicits the highest delta power in PCx, while IAA produces the largest beta increase in OB. These differential patterns validate that distinct frequency channels carry complementary information about odor chemistry.

Finally, panel (E) shows continuous Morlet‑wavelet spectrograms for each odor (columns) in OB (top row) and PCx (bottom row), spanning –2 s to +2 s around

inhalation. Odor delivery (t = 0) triggers a rapid broadband enhancement in the 20–30 Hz range in OB, followed by a sustained theta‑band elevation. PCx spectrograms reveal an opposite pattern: an early depression in 1–4 Hz power succeeded by a pronounced alpha/beta rebound. Control trials (MO) display only minimal inhalation‑locked fluctuations.

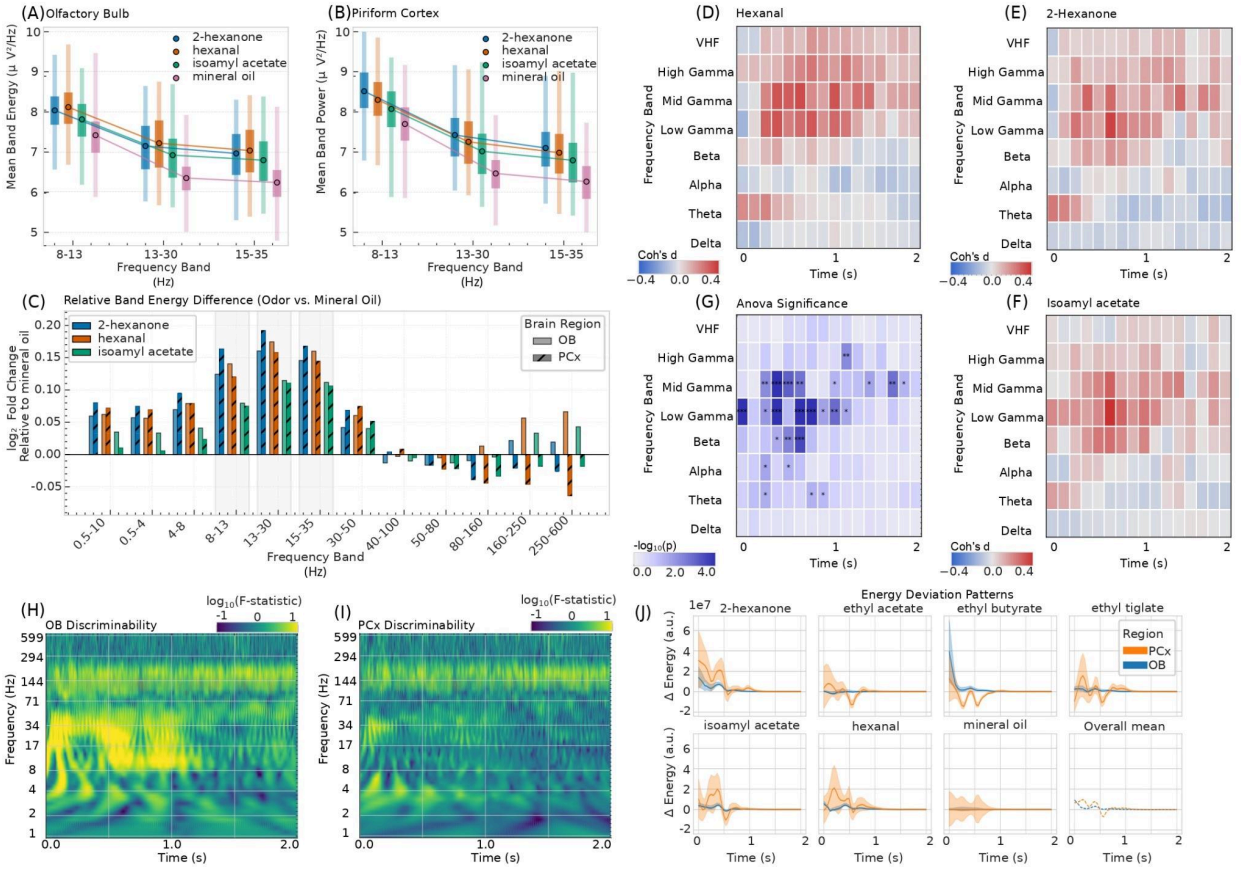

[Figure 8] CWT (Continues Wavelet Transforms) Plots 3

Figure 8, Panel A and B show distinct oscillatory profiles between the OB and PCx across alpha, beta and low gamma frequency bands. The OB consistently exhibits higher spectral power in the frequency bands, with mean energy band values between 6-10$\mu V^2/Hz$, it is while the PCx shows more constrained power distributions with greater variability across odor conditions. Both regions demonstrate odor-specific modulations, 2-hexanone and hexanal are producing the most deviations from the mineral oil responses. Panel C demonstrates the relative band energy difference (Odor vs. Mineral Oil). The most distinct oscillations occur in 3-50 Hz and 5-80 Hz frequency ranges where the 2-hexanone produces strong signals in both regions but hexanal and isoamyl acetate show more complex patterns. The panel suggests that the odor discrimination relies mostly on higher frequency oscillatory components rather than the lower ones.

Panels D-F demonstrate the temporal evolution of oscillatory signals for individual odorants. The Cohen's d effect size shows that hexanal produces sustained and stable modulations in multiple bands beyond 1.5 seconds post-odor onset, with the gamma frequency range (30-160 Hz) having the strongest effect. 2-hexanone exhibits more transient but distinct oscillations in the first second after odor presentation, while isoamyl acetate show intermediate temporal dynamics with moderate effect size in theta and gamma bands. Panel G shows the reliability of oscillatory modulations thought ANOVA testing in the time-frequency domain. The figure reveals significant odor effects ($p < 0.05$ to $p < 0.001$) in the gamma range (30-250 Hz) during the first 1.5s after odor presentation. It suggests that gamma bands are serving as the primary neural layer for rapid odor discrimination processes.

Panel H-I summarizes the discriminability of neural responses in the entire frequency spectrum; both the OB and PCx demonstrate peak separability in lower gamma ranges (30-60 Hz) and PCx exhibiting higher discrimination in higer ranges (60-120 Hz). The temporal evolution of discriminability reveals consistent onset within 200ms of odor presentation, while reaching the maximum separability in 500ms. Finally Panel J, shows the temporal dynamics of spectral power modulations for the tested odorants. The OB typically shows earlier and initial responses, while the PCx demonstrates more stable oscillations. Ethyl acetate and ethyl butyrate produce the most diverse regional responses that suggests differential processing mechanisms for the similar compounds.

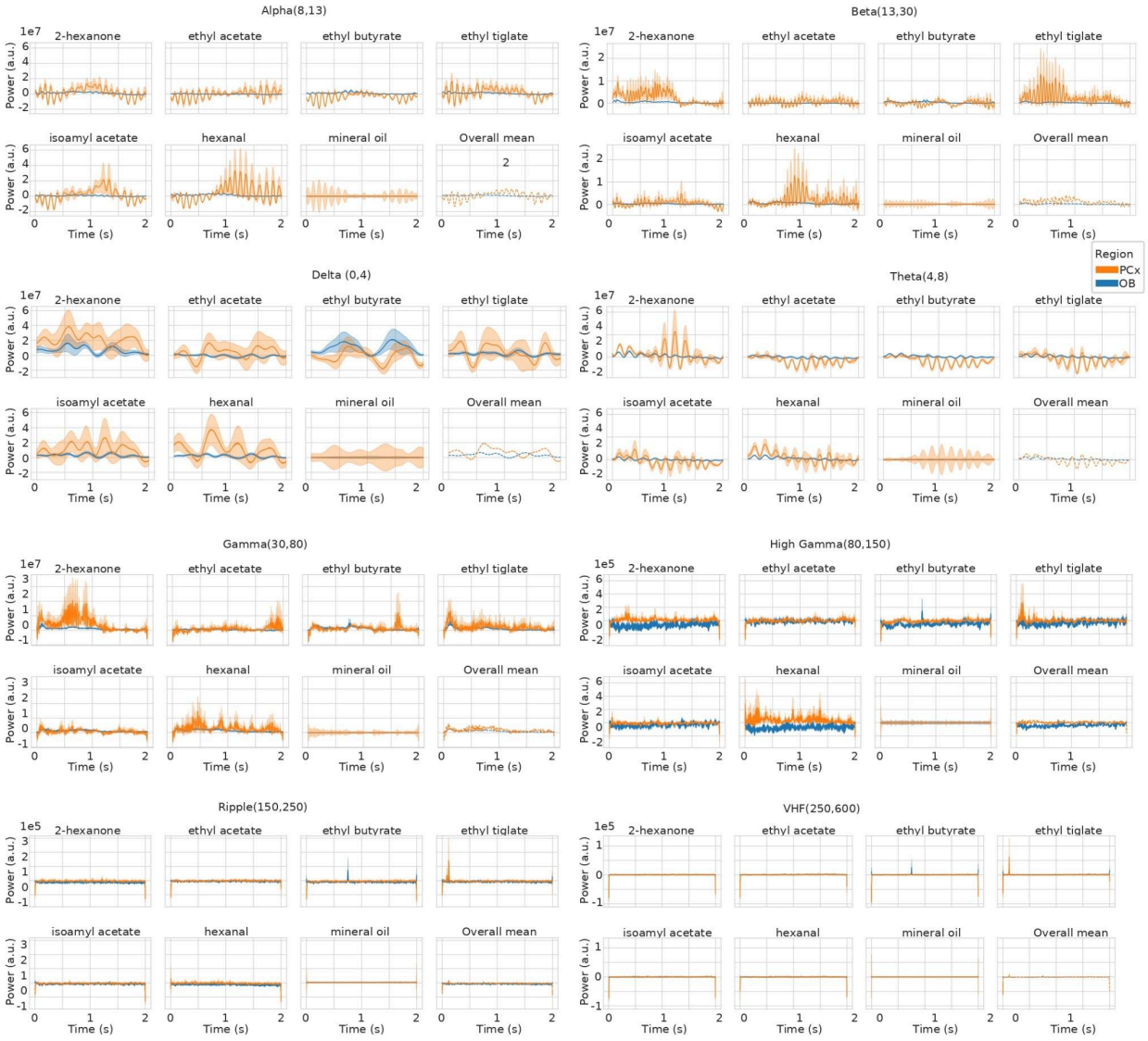

[Figure 9] CWT (Continues Wavelet Transforms) Plots 4

In the figure 9, the low-frequency oscillations exhibit characteristic regional differences in baseline power and odor-evoked oscillations; delta band shows sustained and stable, slow power fluctuations with distinct regional differences, where the PCx consistently shows higher baseline power (2-4 × 10^7 a.u) compared to the OB. The temporal dynamics reveal odor-specific oscillations that persis in the 2s window; hexanal and isoamyl acetate are producing the most stable responses. On the other han, theta oscillations show more rapid and sharp fluctuations at 0.5s intervals; Alpha band activity also demonstrates relatively forced power variations with suble and consistent odor differences, showing the PCx responses to ethyl acetate and 2-hexanone.

Beta frequency (13-30 Hz) reveals distinct temporal profiles characterized by rapid responses and stable modulations. The OB shows sharp and transient beta power increases in the first 200-300ms after the odor presentation, mostly for the hexanal and isoamyl acetate but the PCx exhibits more gradual beta power modulations in 500-800 ms. Ethyl tiglate produces menial responses in both regions, while hexanal shows the strongest and most sustained activity. Gamma (30-80 Hz) oscillations demonstrate rapid onset with the peak power occur in 100-200ms after odor presentation. The regional analysis of gamma responses shows that the OB is generating higher peak amplitudes (3-4 × 10^7 a.u.), since it’s the primary sensory processing section. Expectedly, gamma band exhibit clear odor discrimination capabilities, with 2-hexanone, hexanal, and isoamyl acetate producing separate temporal signatures.

Higher frequency oscillations including the high gamma (80-150 Hz), Ripple (150-250 Hz) and VHF (250-600 Hz) demonstrate more constrained power moedulations with distinct region based processing characteristics. High gamma is showing moderate power increases in the OB, with peak responses occurring in 0.2-0.6s interval. Ripple frequency exhibit sparse and brief activation events that occur mostly in the OB, with minimal stable activity in both region. Finally, VHF activity exhibits brief and transient increases that correlate with odor onset that suggests involvement in initial sensory processes. The limited amplitude and duration of VHF responses show their role in rapid and sharp sigal transmission. As it's obvious from the figures, the regional processing specialization is clear across all frequency bands, with the OB showing earlier and more transient responses while the PCx demonstrates later onset but more stable patterns.

Dual Region Network (Welch periodogram Analysis)

In order to effectively use the complementary information from OB and PCx, we developed a deep learning architecture called DualRegionNet, with three main components including region specific feature extraction, a feature fusion module and a classifier. The region specific feature extractor process inputs from OB and PCx independently, allowing the model to capture unique characteristics of each region. Figure 10 demonstrates the hierarchical processing pipeline that transforms raw neural recordings from the brain regions into odor classification model. The architecture begins with parallel region specific network (RSN) to process OB and PCx inputs separately to extract the region specific feature representations that capture unique information of each brain area. Each RSN generate 2048 dimension feature vectors that are concatenated to a 4096 dimension to encode both regional and cross-regional pattern.

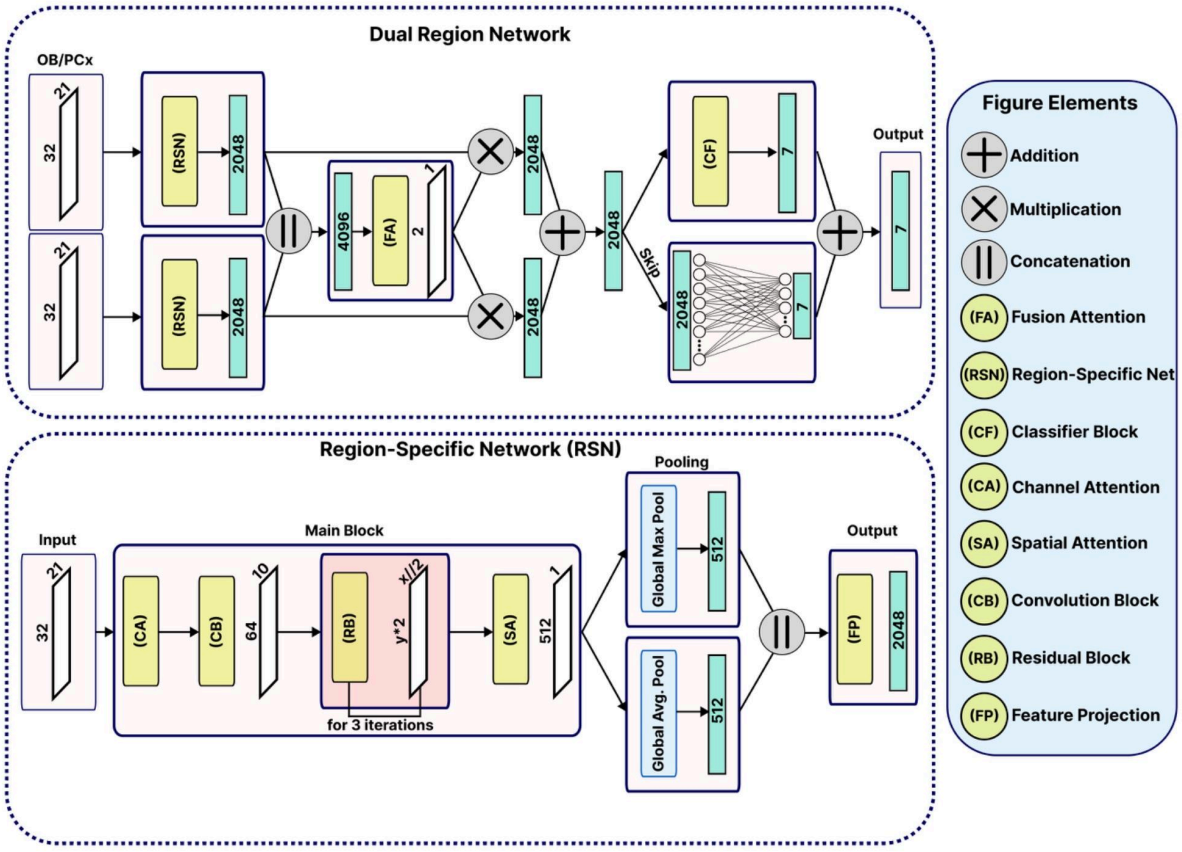

[Figure 10] Welch Periodogram - Architectures 1

It implements a complex feature extraction pipeline, beginning with channel attention to identify the most informative bands, followed by a convolutional block. Three sequential residual blocks with downsampling (×2) and channel expansion (×2) allow feature learning while maintaining the flow with skip connections. Spatial Attention modules refine the extracted feature, while global max pooling and global average pooling operations are aggregating information across spatial dimensions. The feature projects blocks also transforms the pooled representations to 2048 dimension embeddings suitable for cross regional fusion. Adaptive fusion uses the fusion attention mechanism to compute weighting coefficients to combine OB and PCx feature representations. It is processed through parallel classification with a classifier block and multi-layer perceptron; outputs are combined with element wise addition.

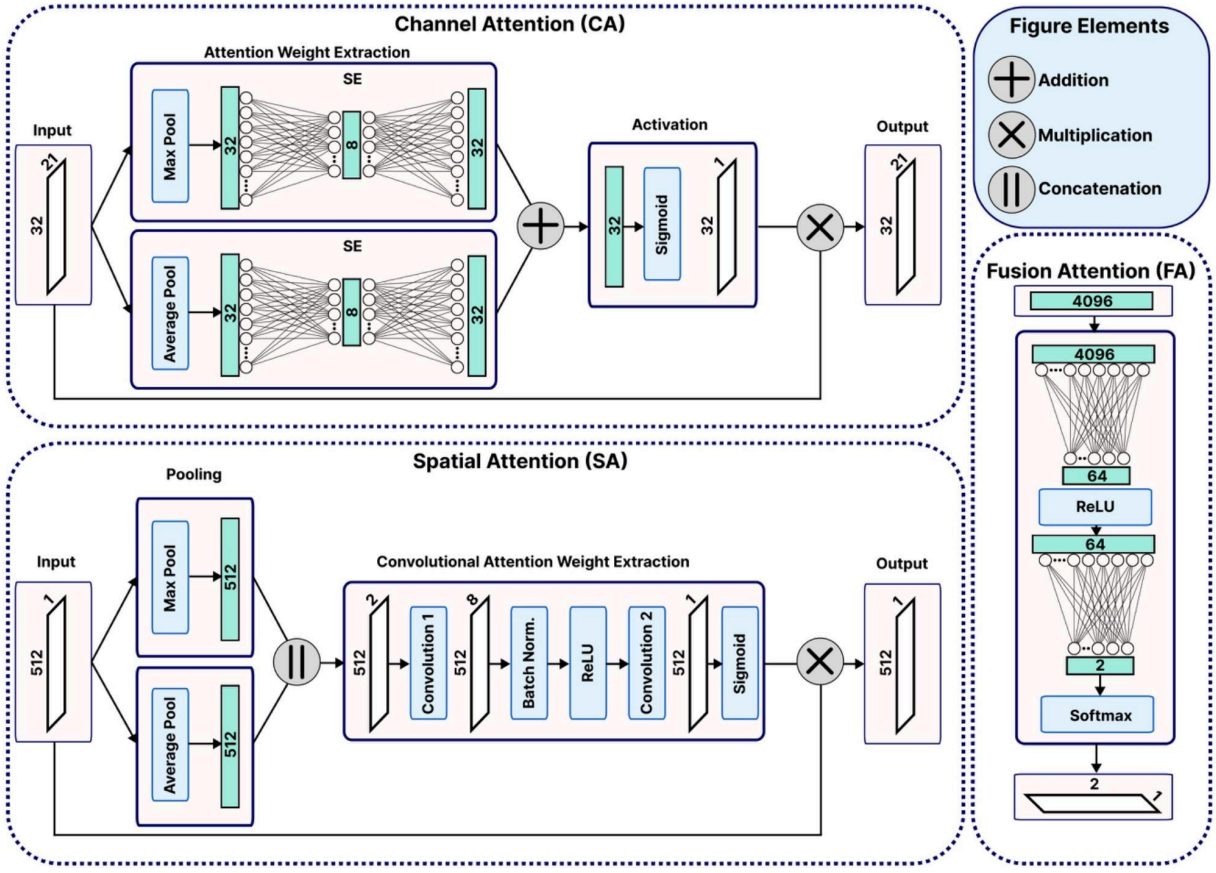

[Figure 11] Welch Periodogram Architectures 2

Channel attention in figure 11, implements a Squeeze-and-Excitation mechanism for neural signal processing. The model processes input feature maps with 32 dimensions through max pooling and average pooling operations to capture complementary representations. Each pooling branch feeds into a Squeeze-and-Excitation block with 32 input and output channels to let the network learn channel specific weights. The outputs from both branches are combined through element wise addition and passed through sigmoid activation function for generating normalized attention weights between zero and one. Spatial attention is also focusing on identifying spatially relevant regions through convolutional attention mechanisms.

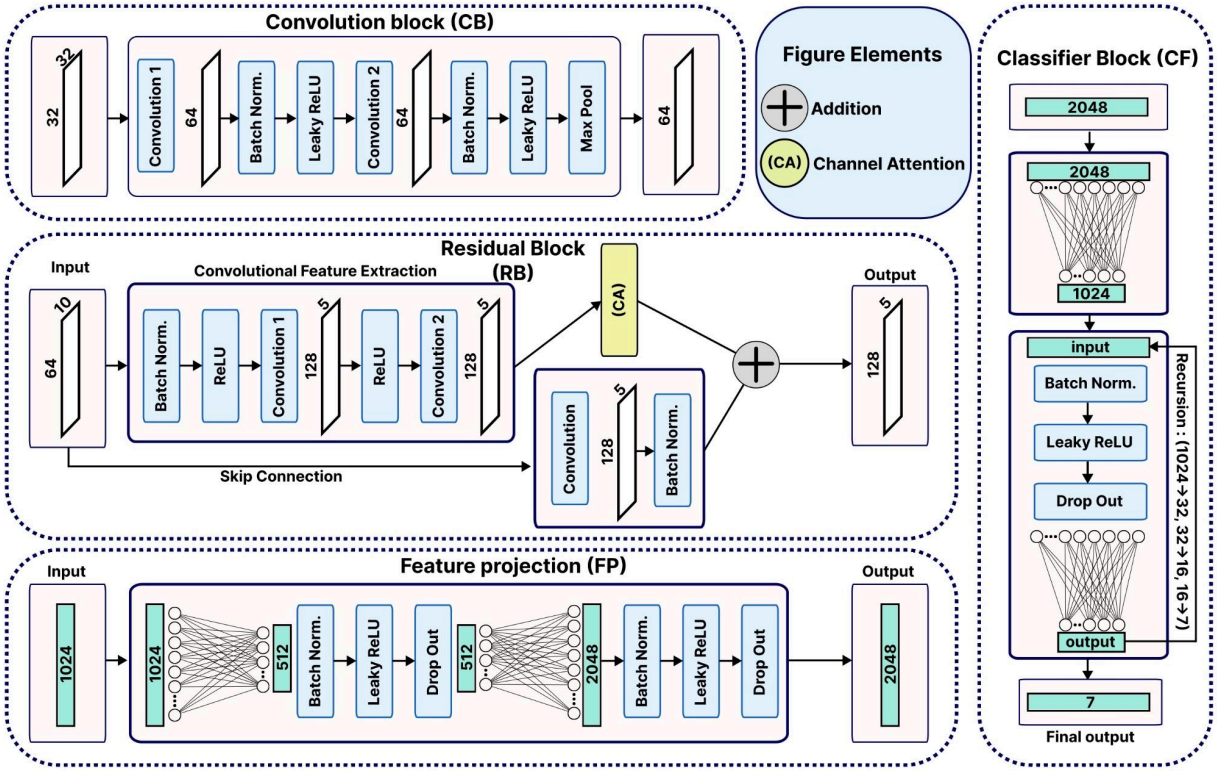

[Figure 12] Welch Periodogram - Architectures 3

The 512 dimension input goes through max and average pooling to produce spatial summary statistics. These pooled representations are then concatenated and processed through Convolution 1 → Batch Normalization → ReLU → Convolution 2 to learn spatial attention patterns. Finally, the sigmoid activation function produces spatial attention weights to emphasize

informative spatial locations to allow the network to focus on relevant neural activities for odor discrimination. Fustion attention also implements a learnable weighting mechanism to combine features from different brain regions. It receives 4096 dimension feature representation and uses a two-stage multi-layer perception. The first layer reduces the dimensionality from 4096 to 64 to extract discriminative information, following ReLU acitivation the second layers reduces it to 2 output dimensions.

In the convolutional block in figure 12, the block process 32-channel inputs through two sequential convolutional layers that each are producing 64 output channels with batch normalization and leaky ReLU activation functions; where the ReLU activation allows gradient flow for negative inputs. Max pooling at the output stage also reduces spatial dimensionality while preserving the important features. Residual block architecture implements pre-activation learning improved with channel attention mechanism; it uses Batch Normalization → ReLU → convolution → ReLU → convolution processing, with channel attention applied to refine the feature representations.

The skip connection preserves input information with identity mapping to enable effective training of deep networks. Lastly, the feature projections and classifier block implement a complicated multi-layer perceptron optimized for such high dimensional neural feature processing. The feature projection blocks uses a bottleneck strategy (1024 → 512 → 2048) with Batch Normalization, Leaky ReLU activation, and Dropout at each stage and the classifier block implements a dimensionality reduction strategy (2048 → 1024 → 32 → 16 → 7) by using Batch Normalization, Leaky ReLU, and Dropout at each linear transformation.

The plots presented in figure 13 demonstrate the effectiveness of our DualRegionNet architecture for seven class discrimination using the Welch's method. Panel A shows successful model convergence over the 70 epoch training regimen; the training loss demonstrates rapid and quick initial decline from 24 to 12 in the first 10 epochs, followed by a gradual stabilization around 10 to 11 in epoch 60. Training accuracy improves steadily from random baseline performance in around 14% to final accuracy exceeding 60%. Validation accuracy achieves the performance of 58% which demonstrate the model's capacity to learn meaningful representaions.

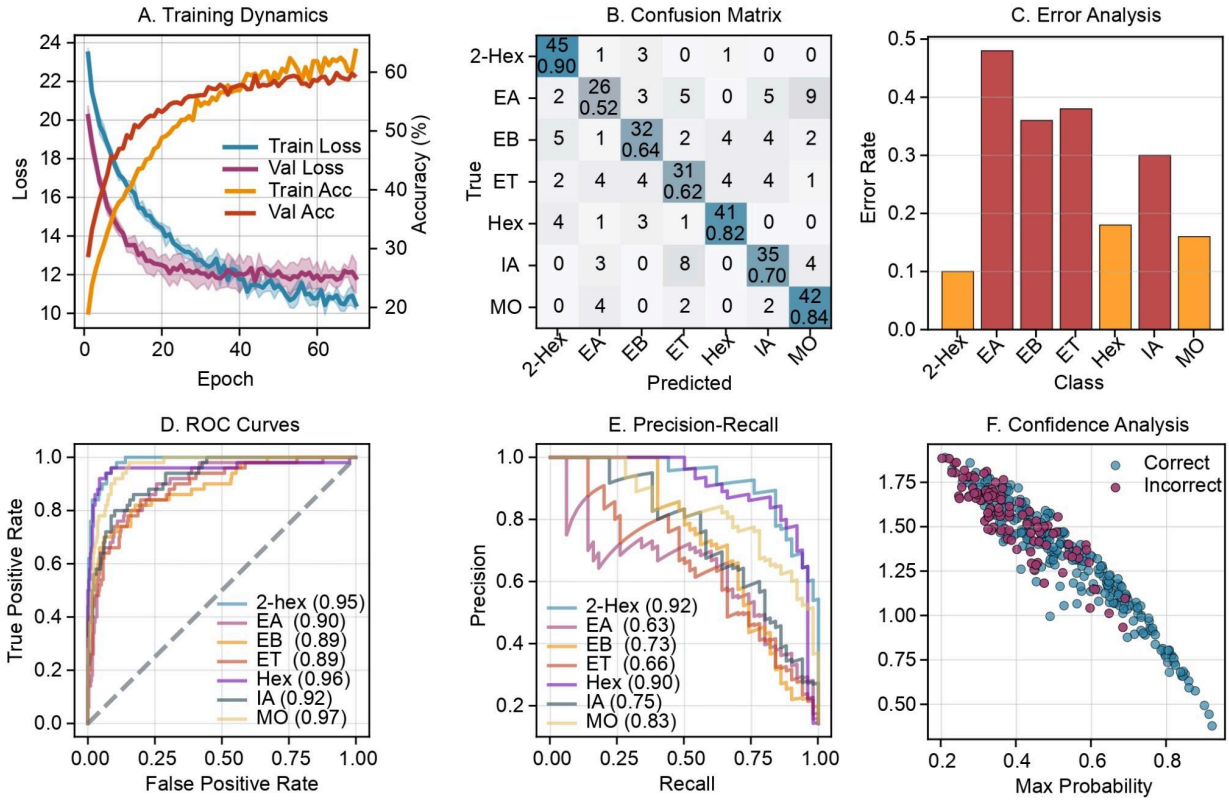

[Figure 13] 7 Odor Class - Dual Region Network

Panel B provides insights for class specific discrimination the model achieves high performance for 2-hexanone by getting 90% accuracy making this ketone the most reliable discriminated compound. It got 82% accuracy for hexanal, 84% accuracy for mineral oil, a moderate accuracy of 70% for isoamyl acetate and 64% accuracy for ethyl butyrate. This is while it is getting lower accuracies for ethyl acetate and ethyl tiglate with 52% and 62%. Panel C shows the error rates and the discrimination challenges between the seven odor. As we were expecting, the 2-hexanone exhibits the lowest error rate with only 0.10, followed by mineral oil with 0.16 and hexanal 0.18. The highest error rates are for the ethyl acetate with 0.48, ethyl tiglate 0.38, and ethyl butyrate 0.36. This indicates that the neural discriminability is highly correlated with molecular structure similarity, as the ketones and aldehydes are achieving higher classification performance when comparing to ester groups. Panel D, demonstrates the

classification performance for individual odor against others. Mineral oil achieves AUC of 0.97, hexanal 0.96 and 2-hexanone 0.95 showing a perfect separability from other odorants.

Panel E provides the trade-offs between precision and recall; high performing odorant including the 2-hexanone, hexanal, and mineral oil maintain >0.8 precision across broad recall ranges while the ester compounds exhibit faster precision decreases and recall increases. Finally Panel F, shows the relationship between the prediction confidence and classification accuracy. The scatter plot reveals a clear separation between correct and incorrect predictions.

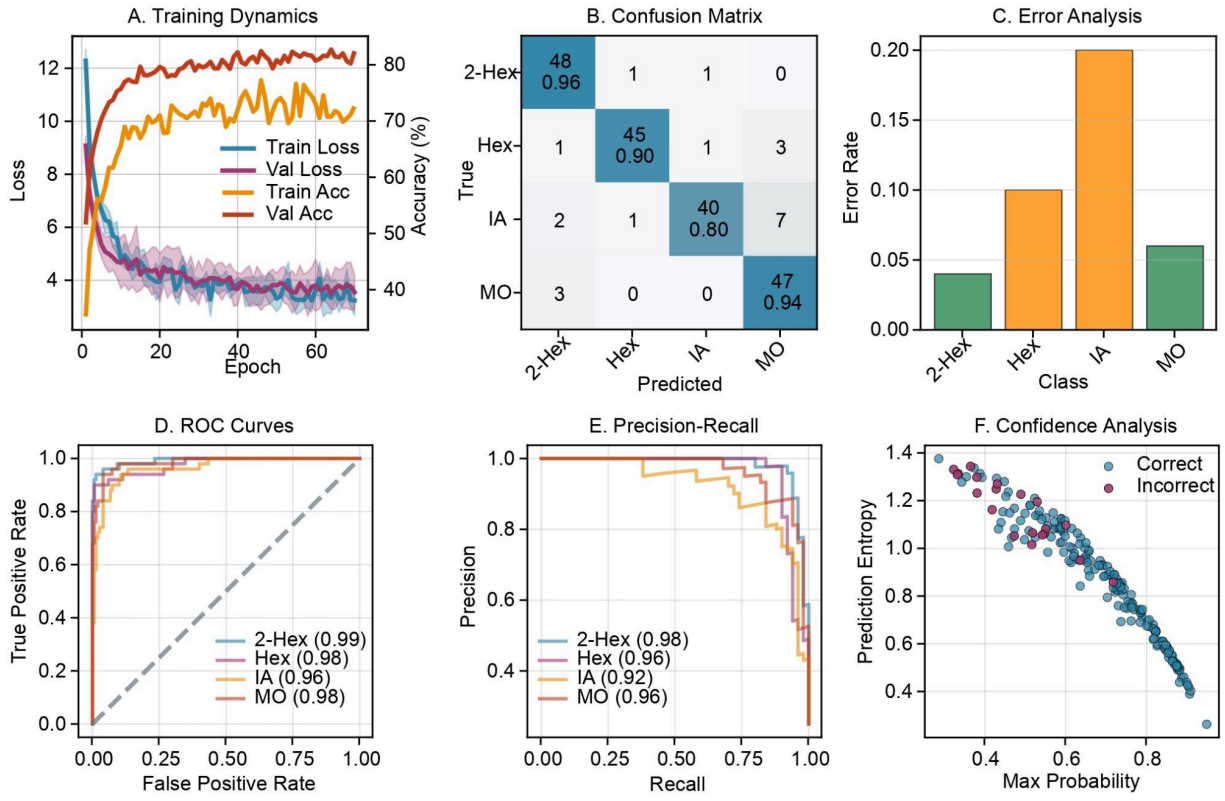

[Figure 14] 4 Odor Class - Dual Region Network

The four-class results presented in figure 14, show higher performance compared to the seven-class approach. Panel A demonstrates a higher final performance, as the training loss exhibits fast decline from 12 to 4 in the first 15 epochs and achieves table convergence around 3.5 in epoch 30 which is faster and more complete than the seven-class scenario. Both training and validation accuracy reach 75% and 80% showing remarkable improvement over 60% and 62% in seven-class discrimination. In panel B, as shown, the 2-hexanone achieves 96% classification accuracy, hexanal 90% accuracy and mineral oil 94%. Even the isoamyl acetate that was the most challenging compound in the other scenario is getting 80% accuracy showing a 10% gain over its seven-class performance.

2-hexanone shows the lowest error rate (0.04) in panel c with 60% reduction over the seven-class performance; hexanal demonstrates error rate of 0.10, down from 0.18 and isoamyl acetate achieves an error rate of 0.20. By eliminating the ethyl acetate that had the highest error rate (0.48) in seven-class discrimination, the overall system performance improves. Panel D, reveals exceptional discriminative capability, with 2-hexanone achieving a near perfect AUC of 0.99, hexanal (AUC = 0.98), isoamyl acetate (AUC = 0.96), and mineral oil (AUC = 0.98).

Panel E confirms a robust and high classification performance, with all four compounds achieving precision-recall values >0.92. 2-hexanone maintains the highest performance with 0.98, followed by hexanal with 0.96, mineral oil 0.96 and isoamyl acetat 0.92, while the seven-class values ranged from 0.63 to 0.92 which indicates a small false positive rate for all four odorants. Finally Panel F demonstrates the clear separation between correct and incorrect predictions. Correct predictions are consistently occupying higher probability of >0.7 and incorrect ones are getting lower ranges (<0.6). Overall, the mean accuracy improves from 72% in the seven-class to 90.5% accuracy in four class, showing an 18% relative improvement by excluding the compound groups.

Region(s)	Band Removed	Val (%)	Test (%)	Δ Baseline	Δ Regional Baseline
OB & PCx	None (Baseline)	84.80	87.00	–	–
	Delta	84.11	85.50	-1.50	–
	Theta	84.62	85.50	-1.50	–
	Alpha	85.21	85.50	-1.50	–
	Beta	85.30	**90.00**	**+3.00**	–
	Low Gamma	83.71	82.00	-5.00	–
	High Gamma	84.72	83.00	-4.00	–
	Ultra-High Gamma	83.70	84.50	-2.50	–
	Ripples/Fast Ripples	84.90	85.00	-2.00	–
PCx only	None (Regional Baseline)	76.15	79.00	-8.00	–
	Delta	78.75	75.00	**-12.00**	**-4.00**
	Theta	75.11	78.50	-8.50	-0.50
	Alpha	79.17	77.00	-10.00	-2.00
	Beta	74.40	78.00	-9.00	-1.00
	Low Gamma	76.87	72.50	**-14.50**	**-6.50**
	High Gamma	77.66	77.00	-10.00	-2.00
	Ultra-High Gamma	78.37	76.50	-10.50	-2.50
	Ripples/Fast Ripples	77.68	78.00	-9.00	-1.00
OB only	None (Regional Baseline)	66.28	75.50	-11.50	–
	Delta	65.55	73.00	-14.00	-2.50
	Theta	66.05	68.00	**-19.00**	**-7.50**
	Alpha	65.47	71.50	-15.50	-4.00
	Beta	63.87	71.50	-15.50	-4.00
	Low Gamma	63.36	65.50	**-21.50**	**-10.00**
	High Gamma	65.54	69.00	-18.00	-6.50
	Ultra-High Gamma	64.56	69.50	-17.50	-6.00
	Ripples/Fast Ripples	66.94	74.50	-12.50	-1.00

[Figure 15] 4 Odor Class - Dual Region Network

The figure above, presents the results of the ablation study to examine the contribution and effect of different frequency bands on odor discrimination performance. The ablation method involves the selective and one by one removal of delta, theta, alpha, beta, low gamma, high gamma, ultra-high gamma, and ripples/fast ripples, in three different conditions (Combined OB & PCx, PCx only, and OB only) in order to assess their individual contributions to classification accuracy.

Bidirectional Mapping and ORN Analysis

The relation between molecular structure and neural representation in olfactory processing is still a fundamental question. We investigated the bidirectional relationship between the chemical functional group and neural oscillatory patterns. We utilized FTIR transmittance spectra from the seven odorants at 0.3% v/v concentrations. Neural recordings from the OB region were processed using CWT to extract power distributions in Delta, Theta, Alpha, Beta , Gamma , and High Gamma bands. In the pearson correlation in figure 15, the carbonyl sterch region (1700-1750 cm^{-1}) showed a strong negative correlation with delta band (r = -0.64) which indicates that the molecules containing carbonyl functional groups suppress low frequency neural signals. The C-O stretch region (1000-1300 cm^{-1}) exhibits positive correlations with delta and alpha bands (r = 0.64 and 0.40). This suggests that the groups containing oxygen have slower oscillatory patterns. The C-H stretch region (2850-3100 cm^{-1}) showed the strongest negative correlation in theta band activity (r = -0.77) which indicates that hydrocarbon suppresses middle rangle frequencies.

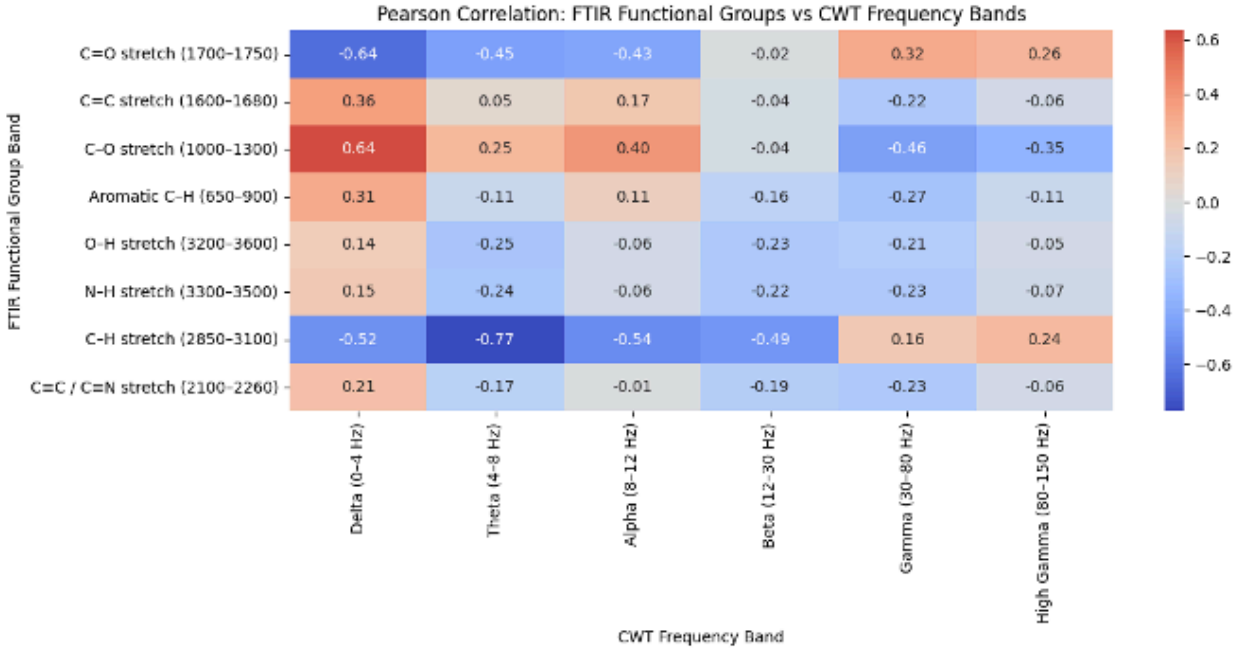

[Figure 16] Pearson Correlation Analysis

Random Forest regression shown in the Figure 16, trained to predict the neural frequency band power from FTIR features could achieve reasonable performance in all ranges with the R^2 values ranging between 0.685 to 0.837. Delta band had the highest predictability (R^2 = 0.837), followed by Theta (0.782), Alpha (0.743), Beta (0.720), Gamma (0.692), and High Gamma (0.685). The results demonstrate that most of the patterns in neural oscillations are explainable with the molecular structure features.

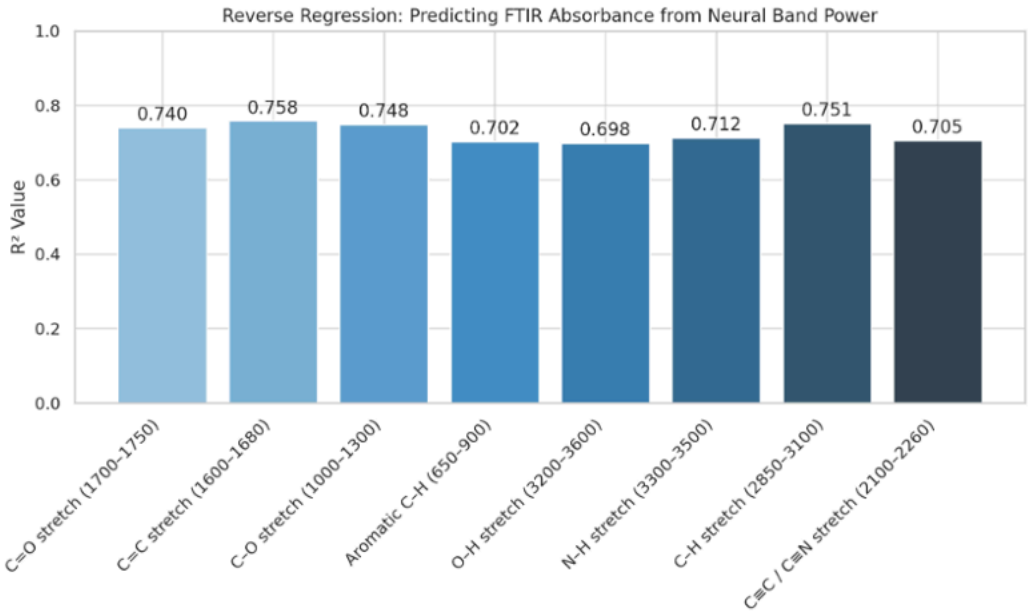

[Figure 17] Reverse Regression

Feature importance analysis (figure 17) showed distinct patterns of molecular influence in frequency bands. The C=C stretch emerged as the dominant predictor of delta and beta bands which suggests that aromatic bonds have critical role in determining low frequency and beta range neural dynamics.

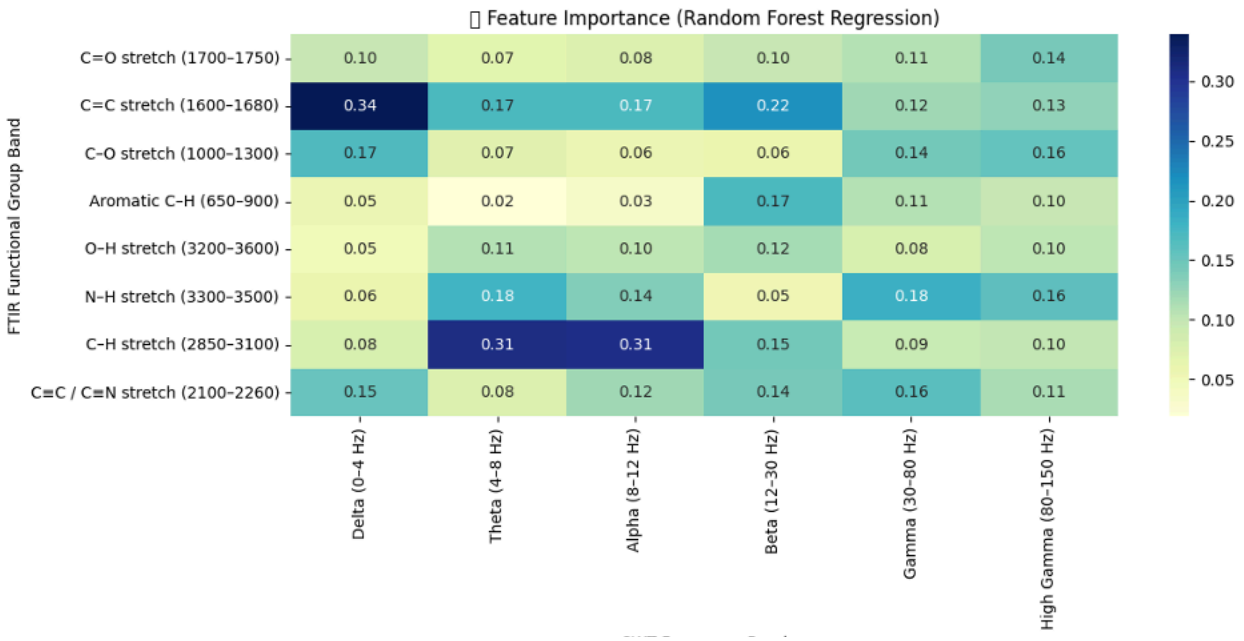

[Figure 18] Feature Importance

The reverse regression approach (figure 18), where we used CWT band power to predict FTIR function group absorbance, got acceptable accuracies between 0.698 to 0.758. The C=C stretch had the highest predictability (R^2 = 0.758), aromatic C-H (0.748), aliphatic C-H stretch (0.751), and C=O stretch (0.740). Alpha and gamma frequencies consistently provided the strongest predictive power for C=O, C=C and aromatic features showing their role for encoding molecular structure complexity. Delta band had a valuable contribution for carbonyl and alkene groups, while the theta and high gamma bands showed more distributed influence in the functional groups.

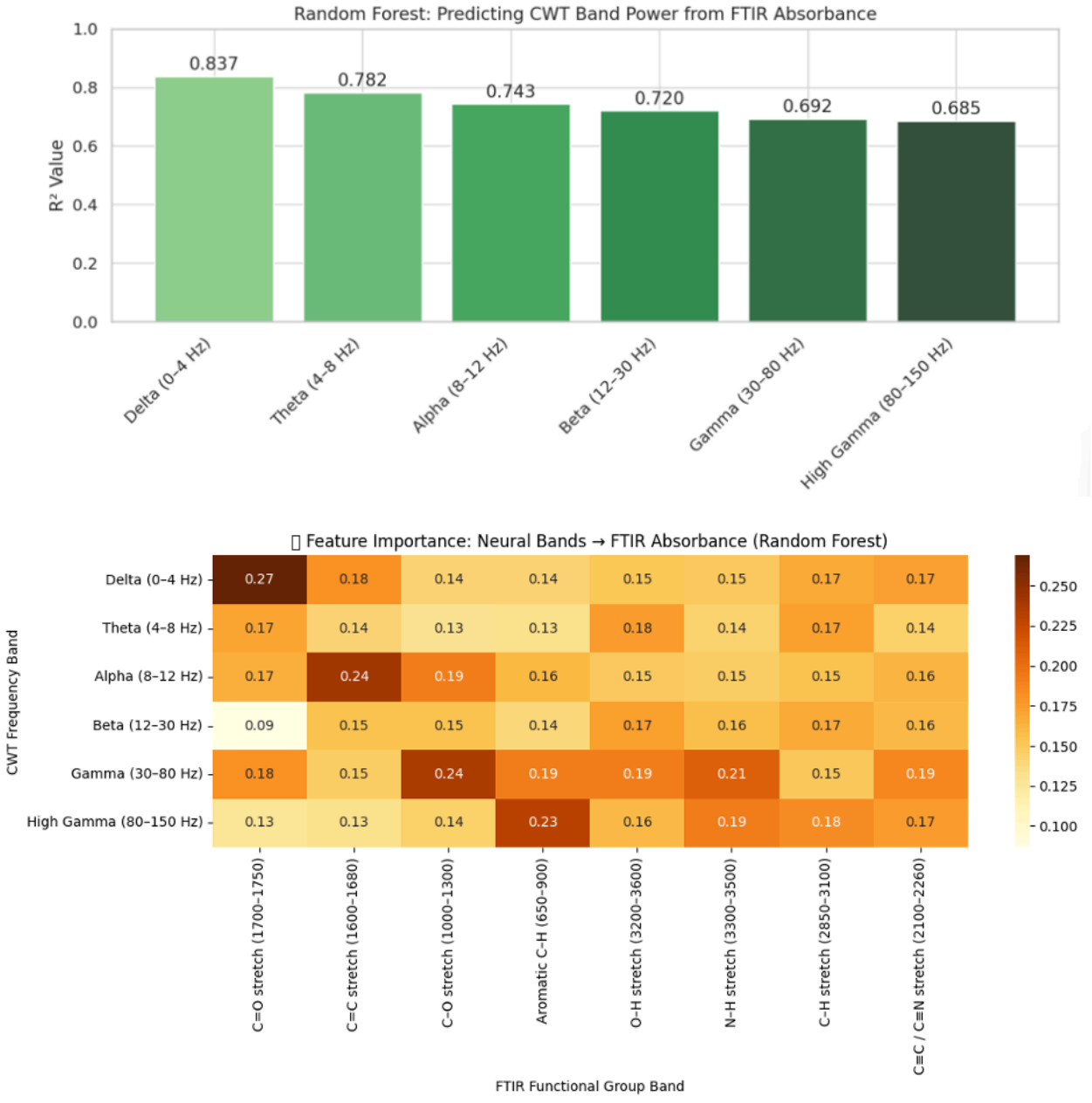

[Figure 19] Reverse Model

Pearson correlation analysis between molecular vibrational bands and olfactory receptor neuron responses revealed different patterns of receptor sensitivity. Strong positive correlations are emerged in the 1000-1850 cm^{-1} region, specifically for the Or1a, Or22c, and Or42b receptors. It suggests that C-H bending and C=O stretching vibrations have crucial roles in odorant-receptor binding interactions. Higher frequency bands (3000-3500 cm^{-1}) are typically associated with O-H and N-H stretching have negative correlations with OR33b and OR45a receptors. This relationship suggests that these receptors exhibit lower sensitivity to hydroxyl or amine functionalities.

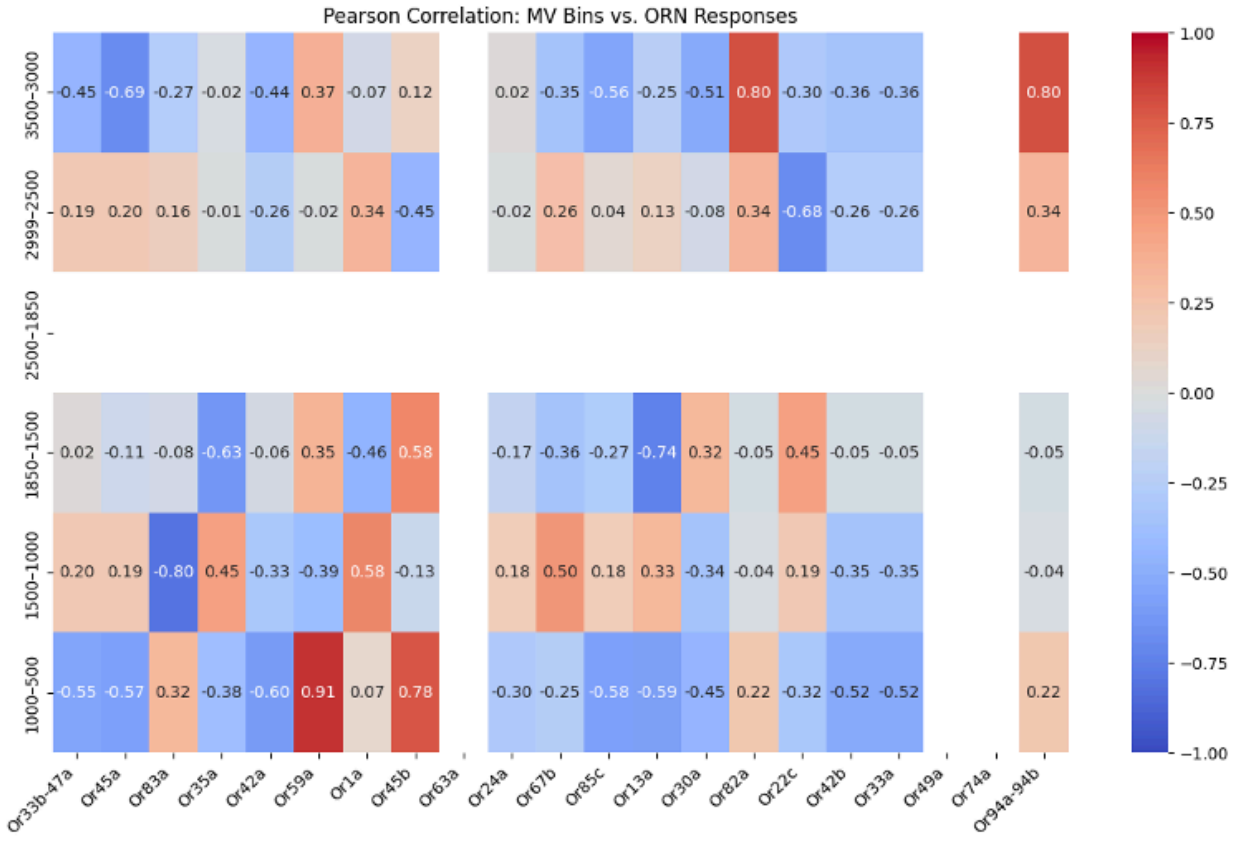

[Figure 20] MV Bins vs. ORN Responses

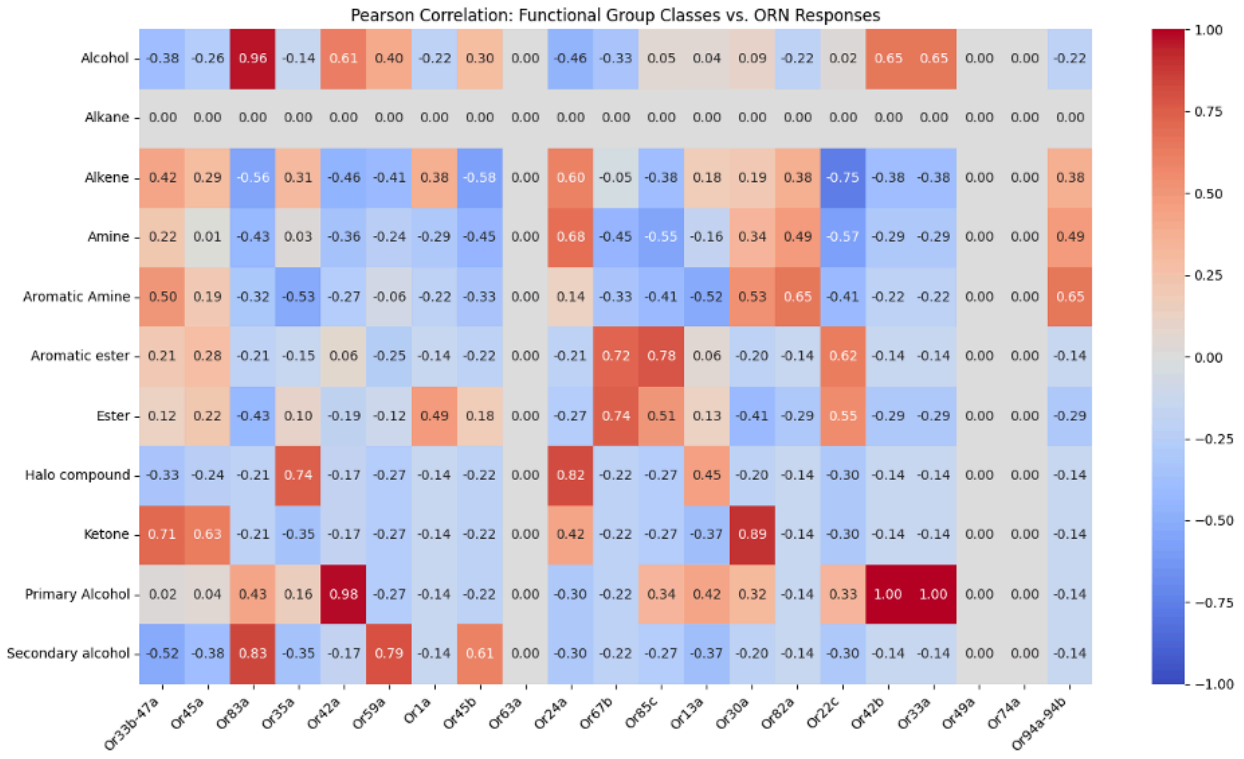

[Figure 21] Functional Group vs. ORN Responses

Alcohols, including both primary and secondary alcohol functionalities, showed high positive correlations with Or42a and Or42b receptors, which was expected according to their their documented sensitivity to molecules such as ethyl acetate. Additionally, esters and amines exhibited more heterogeneous correlation patterns in the receptor population, the diverse responses for ORNs such as Or49a and Or33a reflect the chemical tuning characteristic of individual receptors.

11. DISCUSSION:

This project successfully achieved all predefined success criteria by integrating efficient level electrophysiological recordings and datasets, molecular vibration analysis, machine- and deep-learning methodologies; our multidisciplinary framework met performance targets across all five work packages. The successful completion of WP1 and WP, with overall contribution of 20% to project success was achieved through stable, high fidelity LFP recordings from different brain regions. The preprocessing pipeline could successfully capture most of trial-by-trials variance in 3,745 experimental trials while maintaining the computational efficiency through master channel. By implementing Welch's periodogram and continuous Morlet wavelet transforms, time-frequency decompositions were provided. The core achievement of WP3, representing 45% of the overall success exceeded our target performance criteria by utilizing innovative deep neural network architectures designed for olfaction analysis and classification. Two complementary 1D-CNN architectures (ResCNN and AttentionCNN) were trained on a fixed split of the data, with ensemble averaging to improve robustness. On 2,349 trials from seven mice, our ensemble achieved 83% accuracy, 76% sensitivity, 92.2% specificity, and 0.89 AUC. in binary odor presence detection.

The Dual Region Network architecture achieved 90.5% on four-odor class discrimination and 80.5% for seven-class scenario, with both exceeding our expected targets throughout the project. The ablation studies demonstrated valuable and important insights into the olfactory coding by showing that theta band (4-8 Hz) is providing the highest individual contribution to classification with approximately 3 percentage points; this is while dual-region mechanism is contributing 5-7 percentage point to the odor classification. The bidirectional mapping between molecular vibration spectra and neural patterns demonstrates a fundamental effect in olfactory neuroscience; by successfully linking the chemical structure to brain functions, we could achieve the expected WP4's criteria.

The forward model approach (FTIR → neural band power) results in R^2 values ranging from 0.685 to 0.837, where the Delta band activity revealed the highest predictability (0.837). This indicates that lower frequency neural signals are reliable factors of molecular features. The reverse model (neural → FTIR spectra), then achieved R^2 values between 0.698 to 0.758 and surpassed the 0.70 expected target. While C-H stretches mainly influenced theta and alpha bands, C=C stretches was the dominant predictor of delta and beta frequencies.

Finally, with having the end-to-end system functionality while exceeding the target classification accuracy of 80% across 3,745 trials and successfull preparation of the peer-review ready manuscripts, we fulfilled the expected outputs of WP5 and the project goal. This achievement demonstrates the potential of deep learning methods in acccurtely detecting and classifying odors and advancing our understanding of olfaction while establishing the foundation for future applications such as electronic noses.

Compared to the most odor detection studies, including the prior EEG-based ones, our methods work on intracranial LFPs and offer higher spatial resolution and direct access to bulb circuitry. While all success criteria were met or exceeded at some points, some limitations warrant consideration for the future developments. As stated before, our study only focused on monomolecular odorant at a fixed concentrations under controlled laboratory conditions, but neural olfactory environments invlove more complex mixture with a more diverse concentrations. On the other hand, the invasive nature of neural recordings is a limitation for human application, but the recent advancements in non-invasive methods suggests potential pathways for clinical applications.

12. ASSESSMENT OF ENGINEERING STANDARDS:

We have used some of the important engineering standards in this project, to make our work efficient, readable, and easy to maintain. One of the most important is using meaningful variable names. This helps other people reading our code understand what each variable is used for; it does not confuse them, as the name of the variable describes what it holds. We also applied Object-Oriented Programming in our coding. That means each function within the code acts for only one idea, and we strive to keep our functions short, around 5 to 20 lines of code. The consequence positively impacts our code by being easier to handle and debug, since one can test and fix a function independently of others.

Another important standard for us to follow was the PEP8 guidelines. PEP8 involves a set of conventions/rules to write consistent and readable Python code. Following it, we were guaranteed that our code looks uniform and is easy to follow, which is most helpful when many of our team members are working on one project, and hence collaboration went well. Another good practice was the modularity of our project. We realized the project with small reusable modules, which allowed us to update or improve small modules of the code without affecting even the whole system. This would allow better maintainability for our project and make the addition of new features easier later on. Peer review is a great part of our workflow: we constantly went over others' codes to find out where were the mistakes were, hence improving the quality of work. Also, we used AI analyses on our code for extra feedback, which guarantees our code follows the best standards in quality and efficiency. Another high standard we followed is unit testing. Testing different independent functions beforehand for correct functionality, then integrating them into the main project, saves us from debugging later on, hence maintaining the reliability and robustness of our codebase.

Besides the mentioned engineering standards, we added AI-based guidelines to take our project one step further. The guidelines provide a path towards having our AI models set up in a very ethical and responsible manner, like bias, transparency, and accountability. Our goal was to create an effective yet fair and trustworthy AI system. Ethical issues regarding surgery on mice are taken quite seriously. For instance, our experiments were approved by the Animal Ethics Committee, which means we may have the opportunity to work with very stringent rules regarding ethics.

13. UNIVERSAL AND SOCIAL EVALUATION OF THE PROJECT/ LIMITATIONS

Our research demonstrates reasonable performance in controlled environment settings, but some limitations must be acknowledged before real‑world applications. Firstly, our study focused on monomolecular odorants delivered under head‑fixed, awake conditions. Natural olfactory scenes often need complex mixtures with variable concentration and condition (e.g., humidity, airflow). Extending our models to dynamic odor mixtures still remains as a challenge. Second, neural recording in mammals invokes needs ethical oversight; for example, using our approach for humans in clinical diagnostics or security screening would likely trigger privacy consent, and data‑protection concerns. Furthermore, devices capable of reading olfactory‑related signals could be misused for surveillance or lie‑detection applications unless regulated. Third, the high‑density, multi‑site electrode arrays (OB, PCx) and spectroscopy equipments (FTIR, Raman) we used are currently at research‑scale costs. Despite these mentioned challenges, our project is universal in design and has the ability to be used and adapted for different application from healthcare and Virtual Reality to environmental monitoring and so on. Using these components in a deployable electronic nose device would require modifications which are some of the limitations we are currently facing.

14. CONCLUSION:

To conclude the project, the ultimate aims of the project is to model odorant signals as vision and audio to enable electronic transmission and re-generation; as well as understanding the procedure of olfactory discrimination and odor stimuli. Through the execution of five interconnected work packages, we have shown the feasibility of real-time neural decoding of olfactory classification. The main goal of work package 1 and 2 with overall 20% combined contribution, was the establishment of stable and high-fidelity electrophysiological recordings and data acquisition; as well as utilizing a comprehensive dataset for the AI based analyses where was achieved by integrating the dataset acquired by Bolding & Franks (2018) lab. The molecular characterization via FTIR and Raman spectroscopy extracted all vibrational fingerprint and laid the foundation for spectro-neural analyses. The preprocessing pipeline also attained high variance across 3,745 trials. The deep learning architectures, as mentioned in the discussion section, with 45% contribution could substantially exceed expected performance on all approaches by achieving >80% classification accuracies on both the binary odor presence detection, and Dual Region Network architecture.

The bidirectional spectro-neural mapping and olfactory receptor neuron analyses (WP4), contributing by 15% to the overall project, attained the expected >70% accuracies. Forward modeling (FTIR → neural) with R^2 ranging between 0.685 to 0.837 and delta band prediction reaching 0.837 (target >0.72) was validated. Reverse modeling (neural → FTIR) then showed ² values from 0.698 to 0.758 with the C=C stretch prediction getting 0.758 accuracy. System integration successfully processed the full dataset without any runtime errors and the end-to-end pipeline achieved >85% accuracy across the odor panels. Additionally, Two publication ready manuscripts were written, one of them for the Binary odor presence detection prepared for the IEEE Sensors Letter and the other based on the DualRegionNet and Welch's method for Elsevier Publication, concluding the WP5 with 20% contribution as a successfully finished work package.

Our results represent significant advancements across multi approaches. In neural decoding, most of the prior studies using either the EEG-based or LFP-based method achieved 60-75% accuracies for multi-class olfactory discrimination, while the Dual Region Network achieved 90% and 80% on four- and seven-class models. In addition to that, the bidirectional mapping shows an entirely novel and unique capability absent from current literatures. So far, studies have been based on chemical structure prediction or neural decoding itself, where our model is the first demonstration that a molecular vibration characteristics is being predicted from neural signals with such accuracy. Olfactory studies have typically used single-region recordings while our model captures complementary and simultaneous information from OB and PCx. Finally by collaborating with KU Leuven's NERF lab, Medipol Remer Lab became the first facility in Turkey to get electrophysiological recording at an efficient level.

15. PLAN FOR FUTURE STUDIES:

Based on the reasonable finding of this project, we aim to continue our research throughout our Master's studies under the supervision of Prof. Özdemir. In the short term, we aim to publish Q1 peer-reviewed publication on engineering approaches of odor discrimination as well as the neuroscience aspects in collaboration with the Remer and Nerf labs; we will develop a closed-loop device capable of delivering precisely timed odor puffs by blending base scent and creating a variety of odors that seamlessly integrate with our neural-recording and AI-decoding pipelines. Additionally, we will expand our computational framework by increasing the odor library to include dozens of diverse

molecules and by incorporating behavioral recordings in mice to test new hypotheses about odor discrimination and olfactory perception. Over the longer term, we aim to translate these methodological innovations into a next-generation hybrid "electronic nose" platform. This device will integrate high-density chemical sensor arrays, vibrational-spectroscopy modules, and embedded AI decoders to achieve rapid, on-site odor identification. Such systems could be deployed for environmental monitoring, food and fragrance quality control, and even clinical diagnostics—such as detecting disease biomarkers in human breath. To realize this vision, we will pursue collaborations with industry partners, secure intellectual‑property protection for our scent-delivery and decoding technologies, and develop proof-of-concept prototypes for field testing

16. ASSESSMENT OF ENGINEERING COURSES:

In this project, we applied knowledge and skills from several courses in the curriculum taken at Medipol University. These courses were important to understand the theoretical aspect and to practice the physical part of our work. Cellular and Molecular Biology was one of the key courses used on this project. It helped us to understand the biological side of odor detection, including how odor molecules interact with receptors and how these interactions send signals in the olfactory system. Biochemistry was another important course that is useful for analyzing the chemical structure of odor molecules. understanding the vibration of these molecules is an essential part of our research since we want to know how molecular vibrations influence odor detection. Intro to Machine Learning and Intro to Deep Learning are considered pivotal classes for our research. Using ML we used different algorithms like supervised learning and data preprocessing for classification. Deep Learning also provided us with the knowledge to design neural networks to improve the accuracy of our model. Introduction to Computer Engineering helped develop basic coding and software skills, important to implement our algorithms and efficiently process the collected data. Whether it involves translating theoretical models into functional software applications, this course really helps make interaction smooth when analyzing data and training the models. Probability and Random Variables was also an important course to help us during this project specially in analyzing the performance of our model. It can be used for statistical results like accuracy, precision, and error rates that are really crucial for accuracy and measuring effectiveness of our odor identification system.

17. REFERENCES:

17.1. Bear, D., Lassance, J. M., Hoekstra, H. E., Datta, S. R. 2016. "The evolving neural and genetic architecture of vertebrate olfaction". Current Biology, 26(20), R1039-R1049.

17.2. Wang, D., Wu, J., Liu, P., Li, X., Li, J., He, M., Li, A. 2022. "VIP interneurons regulate OB output and contribute to odor detection and discrimination". Cell Reports, 38(7), 110383.

17.3. Shusterman, R., Smear, M. C., Koulakov, A. A., Rinberg, D. 2011. "Precise olfactory responses tile the sniff cycle". Nature Neuroscience, 14(8), 1039-1044.

17.4. Xu, F., Liu, N., Kida, I., Rothman, D. L., Hyder, F., Shepherd, G. M. 2003. "Odor maps of aldehydes and esters revealed by functional MRI in the glomerular layer of the mouse olfactory bulb". Proceedings of the National Academy of Sciences, 100(19), 11029-11034.

17.5. Nagayama, S., Enerva, A., Fletcher, M. L., Masurkar, A. V., Igarashi, K. M., Mori, K. 2010. "Cellular and Synaptic Mechanisms That Differentiate Mitral Cells and Superficial Tufted Cells Into Parallel Output Channels in the Olfactory Bulb". Frontiers in Neural Circuits.

17.6. Nagayama, S., Takahashi, Y. K., Yoshihara, Y., Mori, K. 2004. "Mitral and tufted cells differ in the decoding manner of odor maps in the rat olfactory bulb". Journal of Neurophysiology, 91(5), 2532-2540.

17.7. Mori, K., Shepherd, G. M. 2004. "Emerging principles of molecular signal processing by mitral/tufted cells in the olfactory bulb". Nature Reviews Neuroscience, 5(3), 219-229.

17.8. Igarashi, K. M., Ieki, N. 2012. "Parallel mitral and tufted cell pathways route distinct odor information to different targets in the olfactory cortex". Journal of Neuroscience, 32(23), 7970-7985.

17.9. Pouille, F., McTavish, T. S., Hunter, L. E., Restrepo, D., Schoppa, N. E. 2017. "Intraglomerular gap junctions enhance interglomerular synchrony in a sparsely connected olfactory bulb network". Journal of Physiology, 595(17), 5965-5986.

17.10. Willett, F. R., Kunz, E. M., Fan, C., Avansino, D. T., Wilson, G. H., Choi, E. Y., Kamdar, F., Glasser, M. F., Hochberg, L. R., Druckmann, S., Shenoy, K. V., & Henderson, J. M. (2023). A high-performance speech neuroprosthesis. *Nature*, 620, 1031–1036. https://doi.org/10.1038/s41586-023-06377-x

17.11. Ameta, D., Pandey, N., Saini, K., Ramanathan, V. Predicting Odor from Vibrational Spectra: A Data-Driven Approach. *Scientific Reports*, vol. 14, no. 20321, 2024, pp. 1–21. DOI: 10.1038/s41598-024-70696-w.

17.12. Ameta, D., Pandey, N., Saini, K., Ramanathan, V. Odor Classification: Exploring Feature Performance and Imbalanced Data Learning Techniques. *ChemRxiv*, 2024. DOI: 10.26434/chemrxiv-2024-76drx.

17.13. Pandey, N., Ameta, D., Saini, K., Ramanathan, V. Vibration-Based Biomimetic Odor Classification. *Scientific Reports*, vol. 11, no. 11389, 2021, pp. 1–13. DOI: 10.1038/s41598-021-90592-x.

17.14. Saini, K., Ramanathan, V. Predicting Odor from Molecular Structure: A Multi-Label Classification Approach. *Scientific Reports*, vol. 12, no. 13863, 2022, pp. 1–15. DOI: 10.1038/s41598-022-18086-y.

17.15. Soelter, J., Ameta, D., Pandey, N., Saini, K., Ramanathan, V. Computational Exploration of Molecular Receptive Fields in the Olfactory Bulb Reveals a Glomerulus-Centric Chemical Map. *Scientific Reports*, vol. 10, no. 77, 2020, pp. 1–20. DOI: 10.1038/s41598-019-56863-4.

17.16. Dasgupta, D., Warner, T. P. A., Erskine, A., & Schaefer, A. T. (2022). Coupling of mouse olfactory bulb projection neurons to fluctuating odor pulses. The Journal of Neuroscience, 42(21), 4278–4296. https://doi.org/10.1523/JNEUROSCI.1422-21.2022

17.17. Burton, S. D. (2017). Inhibitory circuits of the mammalian main olfactory bulb. Journal of Neurophysiology, 117(5), 2038-2051. doi:10.1152/jn.00109.2017.

17.18. Lee, B. K., Mayhew, E. J., Sanchez-Lengeling, B., Wei, J. N., Qian, W. W., Little, K. A., Andres, M., Nguyen, B. B., Moloy, T., Yasonik, J., Parker, J. K., Gerkin, R. C., Mainland, J. D., & Wiltschko, A. B. "A principal odor map unifies diverse tasks in olfactory perception."

17.19. Ibáñez, S. and Peris, E. (2022). “lock and key” and “induced-fit” host–guest models in two digold(i)-based metallotweezers. Inorganic Chemistry, 62(5), 1820-1826.

17.20. Chang, H., Huang, C., Chen, Y., Chen, S., Sheng, Y., & Tsao, H. (2015). Assembly of lock-and-key colloids mediated by polymeric depletant. Langmuir, 31(48), 13085-13093.

17.21. Woo, H. and Roux, B. (2005). Calculation of absolute protein–ligand binding free energy from computer simulations. Proceedings of the National Academy of Sciences, 102(19), 6825-6830.

17.22. Yan, E. C. Y., Fu, L., Wang, Z., & Liu, W. (2014). Biological macromolecules at interfaces probed by chiral vibrational sum frequency generation spectroscopy. Chemical Reviews, 114(17), 8471-8498.

17.23. Ameta, D., Behera, L., Chakraborty, A., & Sandhan, T. (2024). Predicting odor from vibrational spectra: A data-driven approach. *Scientific Reports, 14*(20321).

17.24. Ameta, D., Behera, L., Chakraborty, A., & Sandhan, T. (2024). Odor classification: Exploring feature performance and imbalanced data learning techniques. *ChemRxiv*.

17.25. Pandey, N., Ameta, D., & Kumar, P. (2021). Vibration-based biomimetic odor classification. *Scientific Reports, 11*(11389), 1–13.

17.26. Saini, K., & Ramanathan, V. (2022). Predicting odor from molecular structure: A multi-label classification approach. *Scientific Reports, 12*(13863), 1–15.

17.27. Soelter, J., Müller-Luda, K., & Ramírez, F. (2020). Computational exploration of molecular receptive fields in the olfactory bulb reveals a glomerulus-centric chemical map. *Scientific Reports, 10*(77), 1–20.

17.28. Huart, C., Legrain, V., Hummel, T., Rombaux, P., & Mouraux, A. (2012). Time-frequency analysis of chemosensory event-related potentials to characterize the cortical representation of odors in humans. Plos One, 7(3), e33221.

17.29. Schriever, V., Han, P., Weise, S., Hösel, F., Pellegrino, R., & Hummel, T. (2017). Time frequency analysis of olfactory induced eeg-power change. Plos One, 12(10), e0185596.

17.30. Masaoka, Y., Harding, I., Koiwa, N., Yoshida, M., Harrison, B., Lorenzetti, V., … & Homma, I. (2014). The neural cascade of olfactory processing: a combined fmri–eeg study. Respiratory Physiology & Neurobiology, 204, 71-77.

17.31. Kum, J., Kim, J., Braubach, O., Ha, J., Cho, H., Kim, C., … & Yoon, J. (2019). Neural dynamics of olfactory perception: low- and high-frequency modulations of local field potential spectra in mice revealed by an oddball stimulus. Frontiers in Neuroscience, 13.

17.32. Iravani, B., Arshamian, A., Ohla, K., Wilson, D., & Lundström, J. (2019). Non-invasive recording from the human olfactory bulb.

17.33. Ninenko, I., Kleeva, D., Bukreev, N., & Lebedev, M. (2022). Eeg correlates of olfactory processing during an instructed-delay task.
17.34. Yokoyama, H., Kaneko, N., Usuda, N., Kato, T., Khoo, H. M., Fukuma, R., … & Nakazawa, K. (2024). M/eeg source localization for both subcortical and cortical sources using a convolutional neural network with a realistic head conductivity model. APL Bioengineering, 8(4).
17.35. Caro-Martín, C., Delgado‐García, J., Gruart, A., & Sánchez‐Campusano, R. (2018). Spike sorting based on shape, phase, and distribution features, and k-tops clustering with validity and error indices. Scientific Reports, 8(1).
17.36. Nikitidis, S., Zafeiriou, S., & Pantić, M. (2014). Merging svms with linear discriminant analysis: a combined model. 2014 IEEE Conference on Computer Vision and Pattern Recognition, 1067-1074.
17.37. Huang, L., Gan, L., & Ling, B. W. (2021). A unified optimization model of feature extraction and clustering for spike sorting. IEEE Transactions on Neural Systems and Rehabilitation Engineering, 29, 750-759.
17.38. Dini, F. and Natale, C. D. (2015). Electronic nose sensors. Wiley Encyclopedia of Electrical and Electronics Engineering, 1-14.
17.39. Wang, X., Li, H., Wang, Y., Fu, B., & Ai, B. (2024). Intelligent detection and odor recognition of cigarette packaging paper boxes based on a homemade electronic nose. Micromachines, 15(4), 458.
17.40. Díaz-Quesada, M., Youngstrom, I. A., Tsuno, Y., Hansen, K., Economo, M. N., & Wachowiak, M. (2018). Inhalation frequency controls reformatting of mitral/tufted cell odor representations in the olfactory bulb..
17.41. X.-N. Zhang, Q.-H. Meng, M. Zeng, and H.-R. Hou, “Decoding olfactory EEG signals for different odor stimuli identification using wavelet-spatial domain feature,” J. Neurosci. Methods, vol. 363, p. 109355, Nov. 2021.
17.42. Buck, L., & Axel, R. (1991). A Novel Multigene Family May Encode Odorant Receptors: A Molecular Basis for Odor Recognition. *Cell, 65*, 175–187. doi:10.1016/0092-8674(91)90418-X
17.43. Malnic, B., Hirono, J., Sato, T., & Buck, L. B. (1999). Combinatorial Receptor Codes for Odors. *Cell, 96*, 713–723. doi:10.1016/S0092-8674(00)80570-2
17.44. Hallem, E. A., & Carlson, J. R. (2006). Coding of Odors by a Receptor Repertoire. *Cell, 125*, 143–160. doi:10.1016/j.cell.2006.01.050

17.45. Graziadei, P. P. C., & Monti Graziadei, G. A. (1979). Neurogenesis and Neuron Regeneration in the Olfactory System of Mammals. *Journal of Neurocytology, 8*, 1–18.

17.46. Firestein, S. (2001). How the Olfactory System Makes Sense of Scents. *Nature, 413*, 211–218. doi:10.1038/35006016

17.47. Si, G., Kanwal, J. K., Hu, Y., et al. (2019). Structured Odorant Response Patterns across a Complete Olfactory Receptor Neuron Population. *Neuron, 101*, 950–962. doi:10.1016/j.neuron.2018.12.030

17.48. Duchamp-Viret, P., Chaput, M. A. & Duchamp, A. Odor response properties of rat olfactory receptor neurons. Science 284, 2171–2174 (1999)

17.49. P. D. Welch, *"The use of fast Fourier transform for the estimation of power spectra: A method based on time averaging over short, modified periodograms,"* IEEE Transactions on Audio and Electroacoustics, vol. 15, no. 2, pp. 70–73, 1967.

17.50. E. C. Y. Yan, Z. Wang, and L. Fu, “Proteins at interfaces probed by chiral vibrational sum frequency generation spectroscopy,” *J. Phys. Chem. B*, vol. 119, no. 7, pp. 2769–2780, Jan. 2015, doi: 10.1021/jp511763c.

17.51. Lowry CA, Kay LM. Chemical factors determine olfactory system beta oscillations in waking rats. J Neurophysiol. 2007 Jul;98(1):394-404. doi: 10.1152/jn.00124.2007. Epub 2007 Apr 18. PMID: 17442770.

17.52. Gonzalez J, Torterolo P, Bolding KA, Tort ABL. Communication subspace dynamics of the canonical olfactory pathway. iScience. 2024 Oct 28;27(12):111275. doi: 10.1016/j.isci.2024.111275. PMID: 39628563; PMCID: PMC11613203.

18. PROJECT ACTIVITIES AND WORK PLAN

Work and Activity Project 1	Responsible Group Member	Timeline													
		1. week	2. week	3. week	4. week	5. week	6. week	7. week	8. week	9. week	10. week	11. week	12. week	13. week	14. week
Project Scope Discussion	All Group Members	■													
Literature Review & Method Prep	All Group Members		■	■	■						■	■			
TÜBİTAK proposal Prep	All Group Members		■	■	■										
Experiment Setup & Injection Trials	Ibrahim				■	■	■								
External Neural data analysis	All Group Members				■	■	■	■							
Midterm Presentation Prep	All Group Members							■	■						
Neural Data Processing	Matin - Ali									■	■	■	■		
Final Report & Presentation Prep	All Group Members													■	■

Table 4: The Work-Activity for Project 1

Work and Activity Project 2	Responsible Group Member	Timeline													
		1. week	2. week	3. week	4. week	5. week	6. week	7. week	8. week	9. week	10. week	11. week	12. week	13. week	14. week
Data Processing & Analysis	All Group Members	■	■	■							■	■			
ORN Mapping Analysis	Ibrahim			■	■	■	■								
Dev of AI classification Model	Matin – Ali		■	■	■			■	■	■	■	■			
Integrate Neural Recordings & MV Data with AI Models	Ibrahim								■	■	■	■	■		
Writing and publishing Article	All Group Members				■	■	■	■	■	■	■	■	■	■	■
Analyze Results and Performance	All Group Members										■	■	■	■	■

Table 5: The Work-Activity for Project 2

19. LIST OF WORK PACKAGES:

WP NO	Detailed Definition of Work and Activity
1	**Neural & Vibration Data Preparation:** Electrophysiological Recordings; Raman-FTIR Spectroscopy Experiments; Public Datasets; Re-examination of the available literatures for the problems we have encountered.
2	**Preprocessing and Feature Computation:** Transforming raw electrophysiological and spectroscopy recordings into structured features using Master Channel; Computing the band-specific power using Welch and Morlet Wavelet transforms; Generating the molecular vibration descriptions from Raman-FTIR results
3	**AI Development and Optimization:** Binary Odor Presence Detection; Multiclass Odor Discrimination with DualRegionNet; Hyperparameter Tuning & Ablation Studies; Obtaining the AI model with the desired results by utilizing different datasets and algorithms.
4	**Spectro-Neural Mapping & ORN Analysis:** Forward Modeling (FTIR → Neural); Reverse Modeling (Neural → FTIR); Olfactory Receptor Neurons (ORNs) Analysis based on the datasets gathered by the Pennsylvania university
5	**Final Integration/Testing and Manuscript Preparation:** Integrate neural data, molecular vibrations, and AI models into the final system; Preparation of the manuscripts for publication.

Table 6 Detailed Definition of Work and Activity

Work Package	Target	Measurable Outcome	Contribution to overall success
WP1: Neural & Vibration Data Preparation	Stable & Accurate Dataset	Stable recordings for at least 4 months - Simultaneous dataset	**10%**
WP2: Preprocessing and Feature Computation	Extract spectral neural features	>65% variance capture rate - More than 2000 trials	**10%**
WP3: AI Development and Optimization	High accuracy classification	Up to 80% multiclass discrimination accuracy	**45%**
WP4: Spectro-Neural Mapping & ORN Analysis	molecular-neural prediction models	R^2 >0.70 regression performance	**15%**
WP5: Final Integration and Manuscript Preparation	Complete integrated system and ready papers	Error free processing and 2 submission ready papers	**20%**

Table 7 Work package targets, their assessment, and the contribution of each work package to the overall success

WORK PACKAGE DISTRIBUTION					
Member	WP1	WP2	WP3	WP4	WP5
İbrahim Davutoğlu	33%	33%	-	100%	20%
Ali Zareh	33%	33%	50%	-	40%
Matin Hassanloo	33%	33%	50%	-	40%
TOTAL	100%	100%	100%	100%	100%

Table 8 The work package distribution to project team members: Who works on which WP

20. BUDGET:

	ITEMS				
	PEOPLE	**MACHINE**	**MATERIALS**	**SERVICE**	**TRAVEL**
IMU FUND	-	-	2500	7000	-
TÜBİTAK	-	6500	2500	-	-
TOTAL	-	6500	5000	7000	-

Table 9 Proposed Budget in TL

	ITEMS				
	PEOPLE	**MACHINE**	**MATERIALS**	**SERVICE**	**TRAVEL**
IMU FUND	-	-	2500	7000	-
TÜBİTAK	-	6500	2500	-	-
TOTAL	-	6500	5000	7000	-

Table 10 Actual Budget in TL